DEVELOPMENT OF A PHOTOACOUSTIC MICROSCOPY SYSTEM

by

Esra Aytaç Kipergil

B.S., Teaching Physics, Boğaziçi University, 2009

Submitted to the Institute for Graduate Studies in
Science and Engineering in partial fulfillment of
the requirements for the degree of
Master of Science

Graduate Program in Physics

Boğaziçi University

2012

ACKNOWLEDGEMENTS

Before all else, I wish to acknowledge to my thesis supervisor Assoc. Prof. Mehmet Burçin Ünlü for all his encouragement, relieving guidance and countless time he has spent for me through all my years as a graduate student. One simply could not wish for a friendlier and understanding advisor. Without his generous instruction, this dissertation would not be possible.

I would like to express my sincere gratitude to the mentor of this thesis Hakan Erkol for his valuable guidance for every step of this study. I gratefully acknowledge him for helpful discussions and for his efforts in constituting theoretical basis of photoacoustics. He is not only a mentor but also a precious friend. I feel honored to work with him.

I would like to thank to TÜBİTAK (The Scientific and Technological Research Council of Turkey) for financially supporting my graduate education.

Thanks to my dear friend Mustafa Bozkurt for his sharing through all my graduate education. I am also thankful to my group friends, Nasire Uluç, Ümit Arabul, and Aytaç Demirkıran.

I would also like to thank to my husband for his endless support, and understanding to every aspects of my life.

My special and deepest thanks to my father and my mother for their support, strength, help, and for everything.

ABSTRACT

DEVELOPMENT OF A PHOTOACOUSTIC MICROSCOPY SYSTEM

Photoacoustic microscopy (PAM), as an imaging modality, has shown promising results in imaging angiogenesis and cutaneous malignancies like melanoma, revealing systemic diseases including diabetes, hypertension, coronary artery, tracing drug efficiency and assessment of therapy, monitoring healing processes such as wound cicatrization, brain imaging and mapping. Clinically, PAM has been emerging as a diagnostic tool. Laser parameters (particularly, pulse duration, pulse energy, pulse repetition frequency (PRF), and pulse-to-pulse stability) affect signal amplitude and quality, data acquisition speed and indirectly, spatial resolution. Lasers used in PAM are typically Q-switched lasers, low-power laser diodes, and recently, fiber lasers. The key laser parameters cannot be adjusted independently of each other, whereas microvasculature and cellular imaging, spectroscopic measurements, e.g., have different requirements. We report an integrated fiber laser system producing nanosecond pulses, covering from 600 nm to 1300 nm, developed specifically for photoacoustic excitation. The system comprises of Yb-doped fiber oscillator and amplifier, an acousto-optic modulator (AOM) and photonic-crystal fiber to generate supercontinuum. Complete control over the pulse train, including generation of non-uniform pulse trains, is achieved via the AOM through custom-developed field-programmable gate-array (FPGA) electronics. The entire system is fiber-integrated; guided-beam-propagation renders it misalignment free and largely immune to mechanical perturbations. The laser is unique in that all the important parameters are adjustable: pulse duration (1-3 ns), energy (up to 10 μJ), repetition rate (50 kHz - 3 MHz). Different photocoustic imaging probes can be excited with the ultrabroad spectrum, real-time imaging can be performed thanks to its high PRF, and the pulse energy can be adjusted by means of FPGA circuit.

ÖZET

FOTOAKUSTİK MİKROSKOP GELİŞTİRİLMESİ

Fotoakustik mikroskop araştırmaları, anjiyogenez ve melanoma gibi derialtı kötü huylu tümör görüntülenmesinde, diabet, hipertansiyon gibi metabolik hastalıkların etkilerinin ortaya çıkarılmasında, tedavinin değerlendirilmesinde, yara iyileşmesinin takibinde, beyin görüntülenmesi ve haritalanmasında görüntülenme yöntemi olarak umut verici sonuçlar vaadetmektedir. Fotoakustik mikroskopta kullanılan lazerin, darbe süresi, enerjisi, atımların tekrar sıklığı gibi parametreleri fotoakustik sinyalin genliğini, kalitesini, veri edinme hızını ve dolaylı olarak uzaysal çözünürlüğünü etkilemektedir. Literatürde fotoakustik mikroskop araştırmalarında kullanılan lazerler sıklıkla Q-anahtarlı, düşük güçlü diyot lazerler, ve son zamanlarda fiber lazerlerdir. Lazer parametreleri birbirinden bağımsız olarak ayarlanamamaktadır, fakat mikrodolaşım sistemi, hücresel görüntüleme, spektroskopik ölçümler farklı parametreler gerektirmektedir. Bu nedenle özel olarak fotoakustik mikroskop için nanosaniyeler mertebesinde atımlar üreten, 600 nm ile 1300 nm arasındaki dalgaboylarını yayabilen lazer üretilmiştir. Sistem, Yd katkılı salıngaç, iki yükseltgeç, akusto-optik değiştirimci ve sürekli dalgaboyu üretimi için fotonik-kristal fiberden oluşmaktadır. Dalgalar dizisi üzerindeki kontrol, akusto-optik değiştirimciye bağlanan programlanabilir mantık dizileri (FPGA) vasıtasıyla sağlanmaktadır. Tüm sistem fiber entegre olup mekanik etiklere karşı stabildir. Lazer tüm önemli parametrelerinin, atım süresi (1-3 sn), enerji (10 micro joule'e kadar yükseltilebilir), atım sıklığı (50 kHz- 3 MHz) ayarlanabilir olması sebebiyle eşsizdir. Ultra geniş spektrum sayesinde farklı problar uyarılabilir, yüksek atım sıklığı sayesinde gerçek zamanlı görüntüleme yapılabilir, FPGA devresi sayesinde atım enerjisi ayarlanabilir.

TABLE OF CONTENTS

ACKNOWLEDGEMENTS . . . iii
ABSTRACT . . . iv
ÖZET . . . v
LIST OF FIGURES . . . viii
LIST OF TABLES . . . xi
LIST OF ABBREVIATIONS . . . xii
1. INTRODUCTION . . . 1
1.1. Motivation . . . 1
1.2. Photoacoustic Imaging . . . 8
1.3. Thermal and Stress Confinement . . . 8
1.3.1. Thermal Confinement . . . 8
1.3.2. Stress Confinement . . . 9
1.4. Applications of Photoacoustic Imaging . . . 10
1.5. Image Characteristics in Photoacoustics . . . 15
1.5.1. Spatial Resolution . . . 15
1.5.1.1. Axial Resolution . . . 15
1.5.1.2. Lateral Resolution . . . 17
1.5.2. Contrast Resolution . . . 18
2. THE SOLUTION OF THE PHOTOACOUSTIC EQUATION . . . 19
2.1. Derivation of Photoacoustic Wave Equation . . . 19
2.2. Solution of Photoacoustic Wave Equation for Dirac Delta Pulse Excitation 22
2.3. Solution of Photoacoustic Wave Equation for Gaussian Temporal Profile 28
2.4. Solution of Photoacoustic Equation for Gaussian Spatiotemporal Profile 38
3. DESIGN OF FIBER LASER FOR PHOTOACOUSTIC IMAGING . . . 49
3.1. Purpose . . . 49
3.2. Lasers Used for Photoacoustic Imaging . . . 50
3.3. Fiber Laser Set- Up . . . 55
3.3.1. Oscillator . . . 55
3.3.2. Pre-Amplifier . . . 56

3.3.3. Final Amplifier 58
3.3.3.1. Supercontinuum Generation 59
4. PHOTOACOUSTIC MICROSCOPY 61
4.1. Ultrasound System 61
4.2. System Design 64
5. CONCLUSION 65
REFERENCES 67

LIST OF FIGURES

Figure 1.1. Classification of Biomedical Imaging Modalities [2]. 1

Figure 1.2. Absorption Coefficient Spectra of Endogenous Tissue Chromophores [33]. 10

Figure 1.3. The Effect of Diabetes on Vessels [38]. 11

Figure 1.4. PAM Image and Photography of The Mouse Cortex Vasculature [44]. 13

Figure 1.5. Healing Process of a Laser-Induced Microvascular Lesion [46]. . . . 14

Figure 1.6. Axial Resolution. 15

Figure 1.7. Spatial Pulse Length. 16

Figure 1.8. Transducers of 50 MHz, 10 MHz and 3.5 MHz. 17

Figure 1.9. Lateral Resolution. 18

Figure 2.1. Normalized photoacoustic pressure waves generated inside a spherical object excited by a short laser pulse for a Gaussian temporal profile vs. normalized time observed at different radial positions (a) r=2 R (b) r=4 R (c) r=6 R. 37

Figure 2.2. Normalized pressure wave $\frac{p(r,t)}{p_0}$ vs. normalized time $\frac{v_S t}{R}$ for (a) $r = 2R$ (b) $r = 4R$ (c) $r = 6R$ where $\frac{\tau}{R} = \frac{1}{10}$. 43

Figure 2.3. Normalized pressure wave $\frac{p(r,t)}{p_0}$ vs. normalized time $\frac{v_S t}{R}$ for (a) $r = 2R$ (b) $r = 4R$ (c) $r = 6R$ where $\frac{\tau}{R} = 1$ 44

Figure 2.4. Normalized pressure wave $\frac{p(r,t)}{p_0}$ vs. pulse duration τ_p at $t = 5\,\mu s$ for (a) $\frac{R}{\tau} = 1$ (b) $\frac{R}{\tau} = 5$ (c) $\frac{R}{\tau} = 10$ where $\frac{r}{R} = 2$. 47

Figure 2.5. Normalized pressure wave $\frac{p(r,t)}{p_0}$ vs. P_{peak} at $t = 5\,\mu s$ for (a) $\frac{R}{\tau} = 1$ (b) $\frac{R}{\tau} = 5$ (c) $\frac{R}{\tau} = 10$ where $\frac{r}{R} = 2$ and E=0.2 mJ. 48

Figure 3.1. Absorption Spectrum of Hemoglobin and Oxygenated Hemoglobin around 500 nm [54]. 51

Figure 3.2. Schematic of the Oscillator Setup. WDM: Wavelength-division multiplexer. 55

Figure 3.3. Schematic of the Pre-amplifier Setup. 56

Figure 3.4. The Schematics of Field Programmable Gate Array (FPGA). . . . 57

Figure 3.5. Schematics of Final Amplifier. 58

Figure 3.6. Schematics of Fiber Laser System. 58

Figure 3.7. Supercontinuum Spectrum. 59

Figure 3.8. Generated Supercontinuum. 59

Figure 3.9. Picture of Fiber Laser System. 60

Figure 4.1. Pulse-Echo signal. 61

Figure 4.2. Cable connections for Pulse-Echo operation of Pulser/Receiver with Oscilloscope. 62

Figure 4.3. Pulser/Receiver and Pre-Amplifier. 62

Figure 4.4. Oscilloscope and Pulser/Receiver settings. 63

Figure 4.5. Data Acquisition Card. 63

Figure 4.6. Schematics of PAM System. 64

LIST OF TABLES

Table 1.1. Comparison of imaging modalities [1, 22]. 6

Table 1.2. Comparison of microscopy systems [23]. 7

Table 3.1. Characteristics of Q-Switched lasers and central frequency (CF) of transducers that are used in recent researches [32, 52–61]. 52

Table 3.2. Characteristics of fiber lasers and central frequency (CF) of transducers that are used in recent researches [62–64]. 53

Table 3.3. Characteristics of fiber lasers and central frequency (CF) of transducers that are used in recent researches [26, 65]. 54

LIST OF ABBREVIATIONS

2D	Two-dimensional
ANSI	American National Standards Institute
AOM	Acousto-optic modulator
CS	Coronal suture
CS	Brain cortex surface
CT	Computed tomography
DOT	Diffuse Optical tomography
fMRI	Functional magnetic resonance imaging
FPGA	Field-programmable-gate-array
FPGA	Field programmable gate array
MAPs	Maximum amplitude projections
MCA	Middle cerebral artery
MRI	Magnetic resonance imaging
NA	Numerical aperture
NIR	Near infra-red
NOLM	Non linear optical lo op mirror
OCT	Optical Coherence Tomoraphy
PA	Photoacoustic
PAI	Photoacoustic Imaging
PAM	Photoacoustic microscopy
PAOD	Peripheral vascular disease
PCF	photonic cyristal fiber
PET	Positron emission tomography
PRF	Pulse repetition frequency
PRF	Pulse repetition frequency
R	Radius
RF	Radio frequency
S	Skin surface
sgn(x)	Signum function

Sk	Skull
SNR	Signal to noise ratio
sO2	Oxygen consumption and rates of change in oxygen saturation
SPECT	Single photon emission computed tomography
SPL	Spatial pulse length
SS	Sagittal sinus
T1	The relaxation time in z-direction
T2	The loss of coherence in x-y direction
US	Ultrasound
WDM	Wavelength-division multiplexer
X-ray CT	X-ray computed tomography
Yb	Ytterbium

1. INTRODUCTION

1.1. Motivation

Biomedical imaging is crucial for diagnosing, examining, and treating diseases; therefore has an important role in the improvement of public health. Various imaging modalities are available including X-ray radiography, X-ray computed tomography (X-ray CT), magnetic resonance imaging (MRI) and its derivatives (such as functional and diffusion MRI), single photon emission computed tomography (SPECT), positron emission tomography (PET) and ultrasound. Optical imaging modalities such as optical, confocal, fluorescence microscopy, endoscopy, optical coherence tomography, and multispectral diffuse reflectance have also clinical applications [1].

In general, these imaging modalities could be divided into two groups; structural and functional techniques. The former, image anatomy of tissue constituents; and the latter, presents physiological functionality [2]. The Figure 1.1 shows the classification hierarchically.

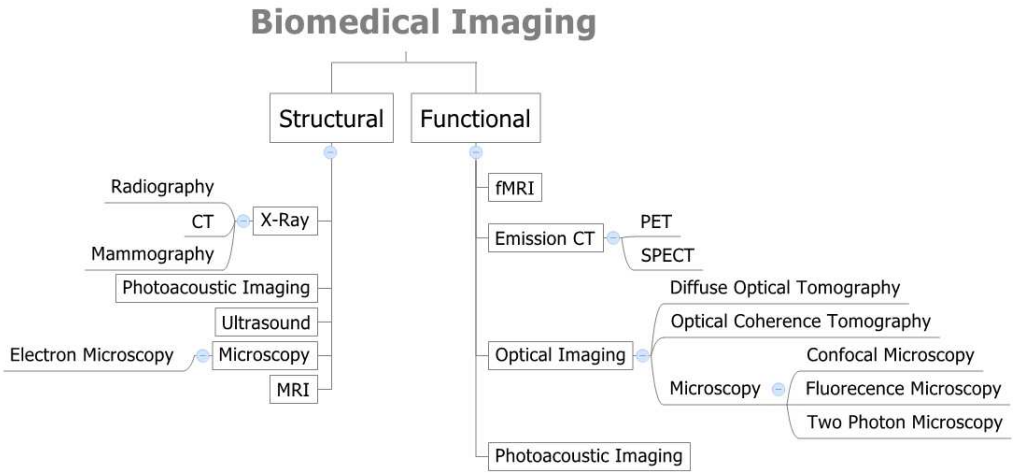

Figure 1.1. Classification of Biomedical Imaging Modalities [2].

X-Ray imaging is one of the most frequently used modalities in clinics. X-Ray CT, based on absorption of X-Rays depicts unattenuated light intensity. CT scanners produce two-dimensional (2D) images using absorption of X-Rays as contrast mechanism from many different angles which are then reconstructed into a three dimensional image. The methodology provides anatomical information non-invasively in a relatively short time with the feasibility of bone and fat imaging. However, X-rays may cause carcinogenesis because of having high electromagnetic energies; and this is the major drawback of the modality [2]. Another disadvantage of the technique is its low spatial resolution (in the order of milimeters) which makes detection of cancer onset impossible. Epithelial tissues that are lucent on a mammogram can hide underlying cancerous lesions especially for high-density breasts of young women [3].

MRI utilizes radio frequency (RF) waves and magnetic fields to acquire three dimensional images. The modality maps the spatial location of protons (mostly hydrogen) present in the tissue of interest. In the absence of an external magnetic field, the direction of the magnetic moments of spinning protons is completely random which causes the net longitudinal and transverse vector to be zero. In the presence of an external magnetic field, a non-zero net longitudinal vector could be created. After RF pulse turned off, the excited nuclei go through a relaxation phase, with two different relaxation times, T1 represents the relaxation time in z-direction and T2 represents the loss of coherence in x-y direction. On the grounds that the voltage signal is spatial location dependent, based on the relaxation times, positional magnetic resonance response of spinning nuclei can be mapped [4]. The usage of non-ionizing radiation makes modality safe for humans. The spatial resolution is better, between 100 μ m and 1 mm, when compared to X-ray CT; however, bone can not be imaged since it does not give an MR signal and appears black as teeth and air. Furthermore, scanning time is relatively long and the equipment tends to be claustrophobic and noisy. It is not suitable for patients with ferromagnetic belongings such as surgical clips, cardiac pacemakers [5]. The major deficit of the technique is that it cannot perform functional imaging without contrast agents. MRI has failed to demonstrate sufficient sensitivity and specificity for breast cancer without contrast agents [6]. On the other hand, contrast-enhanced MRI could be preferred for young women having dense breast with

epithelial tissues that mask cancereous structures under CT [3, 7].

Emission Tomography, classified as positron emission tomography (PET) and single photon emission (SPECT) can provide physiological function information by mapping the absorption coefficient distributions. A radioisotope compound has been introduced into a patient's body which is distributed into various organs and tissues and then the absorbed compounds decay via the emission of positrons. In SPECT, radioisotopes decay with emitting a single gamma photon. In both methodologies, the detector readings are then reconstructed to find initial compound distribution [2]. With the use of contrast agents, in a similar way to MRI; PET is also capable of providing functional information. Although PET is successful at imaging cancers bigger than 1 cm, it has a low sensitivity in identifying lesions below that size [6–9].

Optical imaging modalities utilize mostly the visible light spectrum (from 400 to 700 nm), occasionally the soft ultraviolet and the near-infrared range of electromagnetic radiation to produce visible images. Optical imaging has some advantages over existing radiological techniques. Visible and/or near infra-red (NIR) light used in optical imaging is non-ionizing; thus, is safe for patients and can repeatedly be used. Tissue constituents can be distinguished by optical imaging since they have different optical scattering and absorption characteristics. This difference is used as contrast mechanism in order to enable functional and molecular imaging [10–12]. Due to high correlation between physiological and dynamopathic changes in tissues and optical contrast, optical imaging techniques can detect abnormalities in tissues such as cancer [13]. The modality can also perform functional imaging either with or without contrast agents at tissue and cellular levels non-invasively.

Ballistic photons are used in confocal microscopy and two-photon microscopy, two exemplifications of optical imaging, in order to acquire high spatial resolution. However, photons are scattered with coefficients between 10 cm^{-1} to 100 cm^{-1} depending on the wavelength used. As reciprocal of scattering coefficients, mean free paths are around 1 mm or less in soft biological tissues at visible and near-infrared wavelengths at which multiple scattering also becomes important. Therefore, after one

optical transport mean free path, these imaging techniques are incapable of penetration and achieving high resolution [14]. The equipment is relatively cheap and portable when compared to advanced imaging modality equipments such as CT and MRI.

Optical Coherence Tomoraphy (OCT), another kind of optical imaging, provides a resolution higher than MRI, CT, SPECT, PET, and ultrasound techniques. Coherence pattern between the reference light and reflected light with various angles provided by mirrors is analyzed. The modality may have a resolution in the order of micrometer when the coherence length is sufficiently short. Although the resolution of OCT is much higher than ultrasonic imaging, it cannot penetrate as far [4].

Diffuse Optical tomography (DOT) is based on scattered photons which randomly walk in tissue [15]. The analysis based on inverse problem which is an ill-posed because of high scattering. DOT has higher temporal resolution compared to another functional imaging modality fMRI but it has poor spatial resolution. The use of non-ionizing radiation allows repeated measurements and can be used on young women with dense breast tissue. However, it is restricted to tumors bigger then 5 mm also overestimate size of tumor because of its low spatial resolution [16–18]. By means of DOT, diffuse photons can go beyond optical mean free path, up to several centimeters. However, the deeper the tissue the lower the sensitivity which means poor depth resolution.

Ultrasound imaging is based on reflections of sound waves at the boundaries of tissue constituents where impedance changes. Detection is carried out by transducers containing piezoelectric material that are capable of producing electric signals when excited by ultrasound rays. Transducers are also used in ultrasound transmission since they can also produce ultrasound waves when they are excited electrically. Ultrasonography has also some advantages over other imaging techniques. Besides being non-invasive, no harmful effects have been detected so far. Spatial resolution is high and it can differentiate soft tissues with great ability. The equipment is compact, mobile, and relatively cheap which facilitates its usage as a clinical tool. Real-time imaging and the ability to detect moving internal structures such as a beating heart, and blood flow by means of Doppler-effect make ultrasound imaging favorable [2].

However, reflection is strong wherever at the boundaries impedance difference is high which makes it meaningless to use ultrasonography to examine lung and digestive system containing gas. It can not penetrate well through the bone since absorption is very high. Although, the modality is very successful in differentiating cystic from solid lesions, breast cancer is isoechoic with fat or breast tissue which makes it impossible to differentiate abnormalities [6]. The major downside of the modality is that optical contrast is low [19].

Photoacoustic imaging, which is explained in a detail in subsequent sections, is a recently developed hybrid biomedical imaging modality that combines the advantages of optical absorption contrast with ultrasonic spatial resolution for deep imaging [20]. Photoacoustic imaging is based on absorption of near infra-red electromagnetic waves. The absorption leads to local heating and thermoeleastic expansion which results in production of ultrasonic waves. On the grounds that different biological tissues have different absorption coefficients, it is possible to reconstruct the distribution of optical energy deposition and obtain images by measuring ultrasound signals [21]. The modality has three major forms: computed tomography (which is also known optoacoustic tomography or thermoacoustic tomography), endoscopy, and microscopy which is the focus of this thesis.

Table 1.1 compares the imaging modalities in terms of contrast mechanism, penetration level, spatial resolution, penetration depth, radiation type, and also their capability to perform functional or structural imaging and illustrates the position of photoacoustic imaging among other modalities.

Table 1.2 compares confocal microscopy, two-photon microscopy and photoacoustic microscopy in terms of contrast mechanism, spatial resolution, and imaging depth.

Table 1.1. Comparison of imaging modalities [1, 22].

Modality	Contrast	Penetration	Depth (mm)	Resolution	Radiation	Application
X-Ray CT	Absorption	Organ-Tissue	200	0.5 mm	Ionizing	Structural
MRI	Absorption	Organ-Tissue	150	1000 μm	Non Ionizing	Structural
PET	Absorption	Tissue-Cellular-Molecular	NL	4 mm	Ionizing	Functional
SPECT	Absorption	Tissue-Cellular	NL	6 to 8 mm	Ionizing	Functional
DOT	Scattering	Organ-Tissue	150	1 to 3 mm	Non Ionizing	Functional
OCT	Scattering	Tissue-Cellular	1 to 3	10 μm	Non Ionizing	Functional
US	Scattering	Organ-Tissue	60	300 μm	Non Ionizing	Structural
PAI	Absorption	Organ-Tissue-Cellular	50	2 μm to 700 μm	Non Ionizing	Functional

MRI: Magnetic Resonance Imaging, PET: Positron Emission Tomography, NL: Not limited, SPECT: Single Photon Emission Computed Tomography, US: Ultrasound DOT: Diffuse Optical Tomography, OCT: Optical Coherence Tomography, PAI: Photoacoustic Imaging, I: Ionizing Radiation, NI: Non-ionizing Radiation, S: Structural Imaging F:Functional Imaging.

Table 1.2. Comparison of microscopy systems [23].

Imaging Modality	Contrast	Depth	Resolution
Confocal Microscopy	Scattering-Fluorescence	0.2 mm	1 to 2 μm
Two-Photon Microscopy	Fluorescence	0.5 mm	1 to 2 μm
Photoacoustic Microscopy	Optical Absorption	3 mm	2 to 15 μm

As can be inferred from the tables, photoacoustic imaging comes into prominence with its characteristics of high spatial resolution and contrast, using non-ionizing radiation with the ability of structural, functional and molecular imaging. This thesis presents the design of a novel photoacoustic microscopic imaging system, PAM with a unique fiber laser.

1.2. Photoacoustic Imaging

Photoacoustic effect was first presented by Alexander Graham Bell in 1881 [24]. Although the effect was discovered long before, the improvements in ultrasonic transducer, computer, and laser technologies made its application as an imaging modality recent.

In photoacoustic imaging, the tissue is excited by a short laser. The duration of the laser pulse should be less than heat relaxation time so that heat diffusion could be neglected and the only interaction mechanism between light and tissue could be considered as absorption. The absorbed light leads to a thermal expansion in tissue which induces a pressure wave. The pressure wave could also be generated by electrostriction when the tissue is exposed to electromagnetic radiation, yet sound generation by thermal effect is the dominant mechanism within the tissue [25]. A continuous wave laser can also generate photoacoustic waves; however, the peak amplitude of the induced PA wave will be smaller because of the less efficient stress confinement coefficient [26]. Ultrasonic detection can be employed either by a focused transducer or a detector array. These signals are then analyzed by using digital signal processing methods to reconstruct the spatial information about tissue structures differentiated with optical absorption characteristics [13, 27].

In order to generate photoacoustic waves thermal confinement and stress confinement conditions must be met [28].

1.3. Thermal and Stress Confinement

1.3.1. Thermal Confinement

Thermal confinement occurs when the laser pulse duration is much shorter than the thermal relaxation time [29]. Energy deposition happens faster than heat relaxation so that heat diffusion can be neglected [30]. Heat diffusion time, τ_{th} in seconds, given

by

$$\tau_{th} = \frac{d_c}{4\alpha_{th}} \tag{1.1}$$

where d_c is the characteristic length or light penetration depth, and $\alpha_{th}(\text{mm}^2/\text{s})$ is the thermal diffusivity or thermal conductivity constant of the medium with an approximate value of 0.1 mm^2/s for tissue [20].

1.3.2. Stress Confinement

Stress confinement occurs when the laser pulse duration is much shorter than the stress relaxation time. Heat conduction and stress propagation is negligible during the laser pulse [28]. A short laser duration will ensure that the pulse will cease before the acoustic wave travels, and that the surrounding tissue will not damage tissue by diffusing the heat. The stress time, τ_s in seconds is given by

$$\tau_s = \frac{d_c}{v_s} \tag{1.2}$$

where v_s is the speed of sound [20].

Pulse duration should be less than stress confinement time which should be less than thermal confinement time [20]

$$t_{pulse} < \frac{d_c}{v_s} < \frac{d_c}{4\alpha_{th}}. \tag{1.3}$$

For 15 μm thickness, thermal and stress confinement times are approximately 4 ns and 10 ns, respectively.

1.4. Applications of Photoacoustic Imaging

Photoacoustic microscopy can be used for various biomedical applications. Photoacoustic imaging uses different absorption coefficients of tissue components as contrast mechanism. Melanin, oxyhemoglobin, and deoxyhemoglobin gives different signals, excluding isosbestic points, due to having discrete absorption coefficients [31,32]. The binding of oxygen to hemoglobin, changes the light absorption spectrum of the molecule. Figure 1.2 shows absorption spectrums of oxygenated hemoglobin (HbO2), deoxygenated hemoglobin (HHb), water, lipid, melanin, collagen, and elastin.

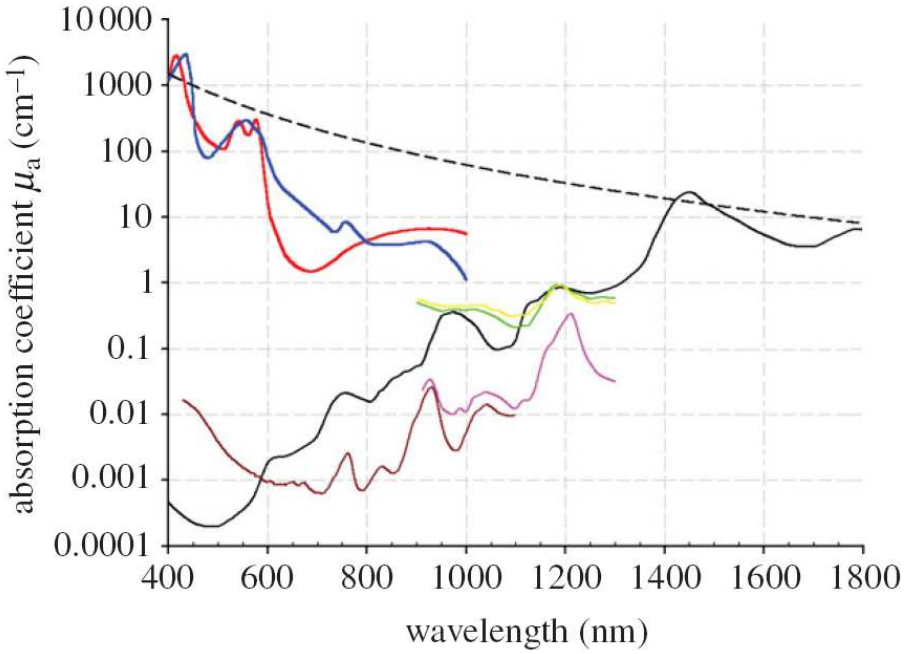

Figure 1.2. Absorption Coefficient Spectra of Endogenous Tissue Chromophores [33].

Oxygenated hemoglobin (HbO2): red line, deoxygenated hemoglobin (HHb): blue line, water: black line, lipid(a): brown line, lipid(b): pink line, melanin: black dashed line, collagen: green line and elastin: yellow line.

The vessels can be distinguished from surrounding tissue by courtesy of hemoglobin when the tissue is exposed to laser light with a wavelength that absorption coefficient of hemoglobin prevails other absorbers' coefficients. Thus, new vessel growth and recovery of vessels after injury, oxygen saturation, the flow of blood in vessels, and the oxygen consumption rate can be imaged [34–36].

The effect of diabetes on vessels can be monitored by means of PAM. The disease causes discernible structural changes on vessels such as decreased diameter, occlusion, increase in the blood flow speed in the vein and a decrease in the artery [37]. PAM can be used to assess how treatment will effect these changes and to propose new remedies or to enable better treatments. Diseases such as diabetes mellitus, coronary artery disease, hypertension, atherosclerosis, arteriosclerosis, and peripheral vascular disease affect the microcirculation negatively [38]. Figure 1.3 shows the effect of diabetes on vessels.

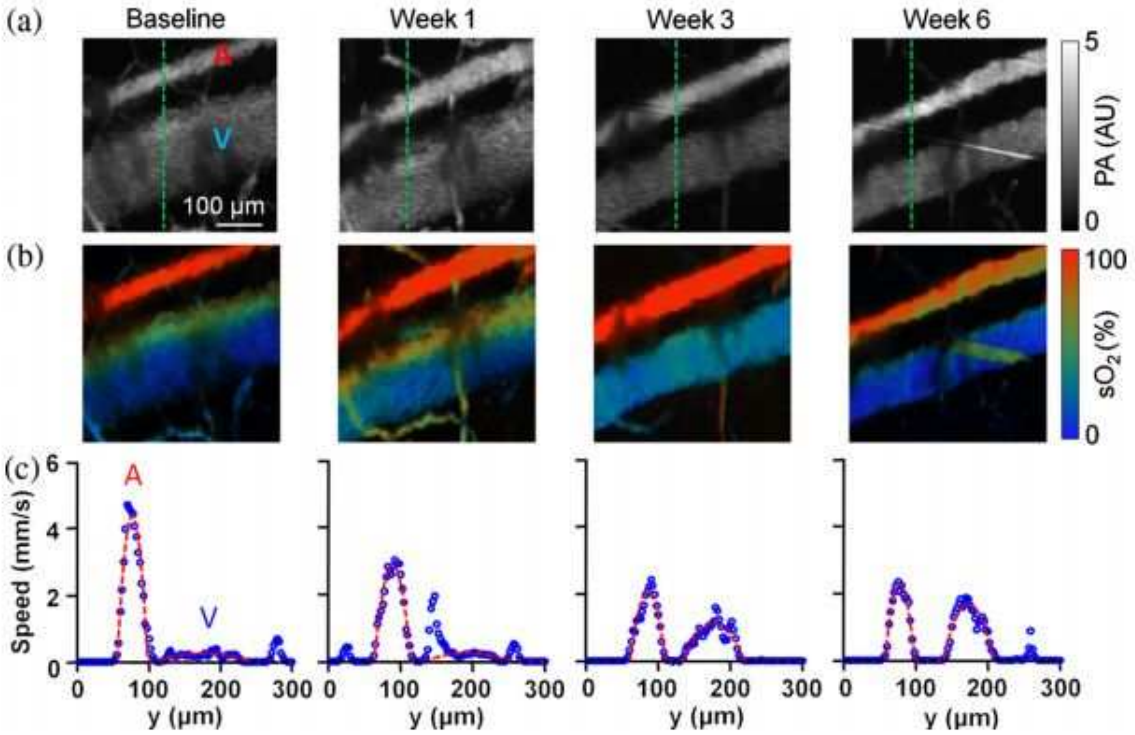

Figure 1.3. The Effect of Diabetes on Vessels [38].

Representative results for one streptozotocin-induced diabetic mouse showing (i) structural photoacoustic maximum amplitude projections (MAPs) through six weeks, (ii) sO2 MAPs of oxygen saturation in the main artery-vein pair studied, and (iii) fitted flow speed profile through a cross section of the main artery-vein pair. A: artery, V: vein.

Oxygen consumption and rates of change in oxygen saturation (sO2) can be measured and compared between healthy people and the ones with peripheral vascular disease (PAOD) by means of PAM with better spatial resolution than near-infrared (NIR) spectroscopy and laser Doppler flowmetry. As a response to ischemic event, vessel dilation and blood flow of healthy people increases more than ten times compared to resting conditions. For people with peripheral vascular disease, the increase is conspicuously less than normal people; thus PAM, can be used as a decision tool in diagnosing peripheral vascular disease [39–43].

Neuronal activity induces hemodynamic response such as the changes in blood oxygenation, volume, and flow of local brain regions. PAM can monitor hemodynamic response as long as it overcomes the acoustic impedance mismatch between skull and surrounding soft tissue and acoustic attenuation of photoacoustic waves propagating through the skull. It is suggested by many researchers that skull reflection coefficient is drastically reduced at the largest incident angles compared to normal incidence and the transmission of PA waves through the skull increases with incident angle. Wang's team created an alternative detector to eradicate this problem. By using high NA acoustic lens to capture more acoustic energy and to increase the acceptance half-angle and by forming annular ultrasonic detection to get rid of reverberations, as can be seen from Figure 1.4 PAM can noninvasively image mouse brain [44].

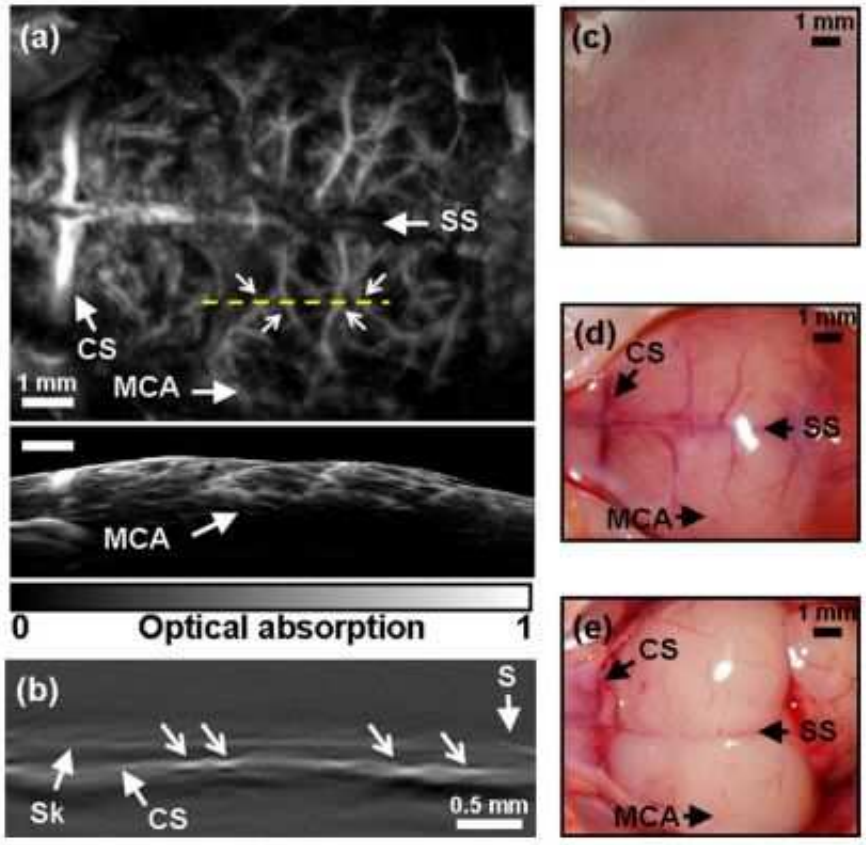

Figure 1.4. PAM Image and Photography of The Mouse Cortex Vasculature [44].

(i) Noninvasive in vivo PAM image of the mouse cortex vasculature. SS: sagittal sinus; MCA: middle cerebral artery; CS: coronal suture. (ii) B Scan denoting depth profile along dotted shown line in a. Arrow heads depict cortex vessels viewed in cross section. S: skin surface; Sk: skull; CS: brain cortex surface. (iii) Photograph taken prior to imaging, when the cortex vessels are invisible to the naked eye. (iv) Photograph taken after image acquisition and scalp removal. (v) Photograph taken after image acquisition and skull removal, showing an unobstructed view of the cortex vessels.

Remedial processes for wound healing including cell proliferation and synthesis of collagen requires the existence of extra oxygen [45]. It is also observed experimentally by many researches that wound healing is delayed under hypoxia which is deprivation of adequate oxygen supply. The Figure 1.5 represents a healing process of a laser-induced microvascular lesion. Hypoxia facilitated angiogenesis and growth of new capillaries to fix the microcirculation can clearly be observed.

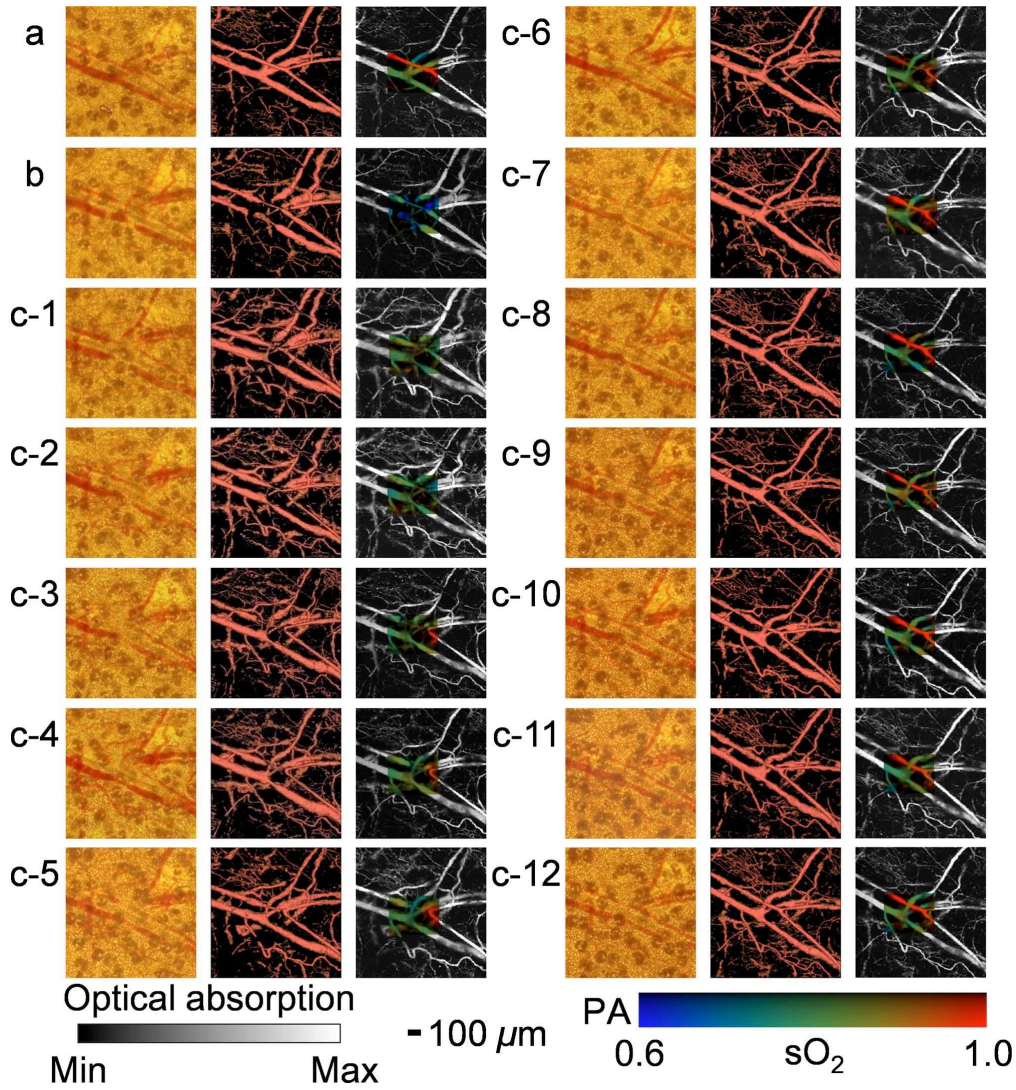

Figure 1.5. Healing Process of a Laser-Induced Microvascular Lesion [46].

1.5. Image Characteristics in Photoacoustics

The overall quality of photoacoustic image is the end product of the all components of the imaging system, including the laser, the transducer, the electronics, and the scanning. In this section, the parameters defining the quality of photoacoustic image which are centered around resolution are explained.

1.5.1. Spatial Resolution

Spatial resolution of an imaging modality can be defined as its ability to distinguish and identify objects as separate in space and itself is divided into axial resolution and lateral resolution. Spatial resolution of photoacoustic imaging is determined by its ultrasound component.

1.5.1.1. Axial Resolution. Axial resolution of ultrasound, also known as longitudinal or azimuthal resolution, is the ability to distinguish reflectors along the axis parallel to the ultrasound beam [47]. Figure 1.6 depicts axial resolution.

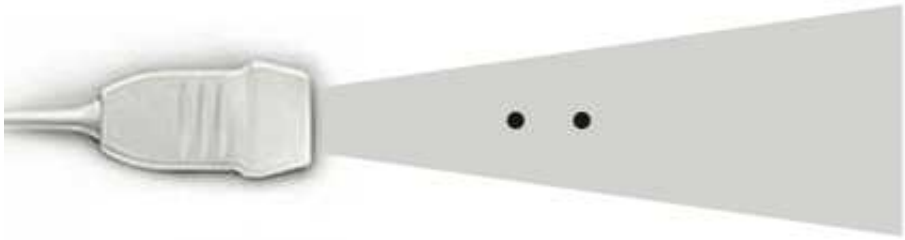

Figure 1.6. Axial Resolution.

Axial resolution is determined by the spatial pulse length and can be formulated by the following equation;

$$\text{Axial Resolution } = \frac{SPL}{2} \tag{1.4}$$

where SPL represents spatial pulse length which is equal to the number of cycles in the pulse multiplied by the wavelength.

$$SPL = \text{number of cycles in pulse} \times \text{wavelength.} \tag{1.5}$$

Shorter spatial pulse length means better axial resolution; that's why damping materials absorbing ultrasound is placed at the back of the piezoelectric crystal. Figure 1.7 illustrates amplitude change versus distance and indicates spatial pulse length.

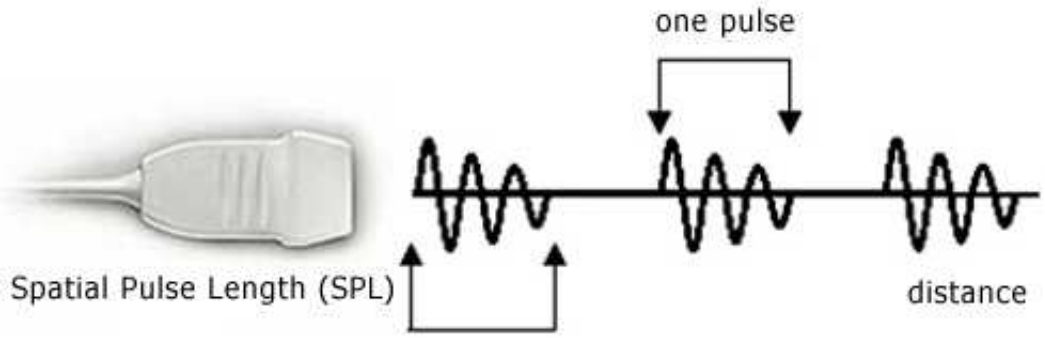

Figure 1.7. Spatial Pulse Length.

Spatial pulse length is proportional to wavelength which is inversely proportional to beam frequency; therefore, higher beam frequency means better axial resolution. On the other hand, sound waves of higher frequency attenuates more since acoustic attenuation is expressed as 0.6 dB/cm/MHz [48]. Spatial resolution can be increased at the expense of imaging depth. Transducer parameters that effect spatial resolution can be summarized as: damping that determines the SPL and the frequency that

identifies the wavelength. Figure 1.8 shows transducers of 50 MHz, 10 MHz and 3.5 MHz, respectively.

Figure 1.8. Transducers of 50 MHz, 10 MHz and 3.5 MHz.

1.5.1.2. Lateral Resolution. Lateral resolution of ultrasound is the ability of transducer to distinguish reflectors along the axis perpendicular to the ultrasound beam [47]. Beam width and beam frequency are main determiners of the lateral resolution.

Reflectors closer than the beam width can not be resolved. Therefore, narrower beam width means better lateral resolution. The lateral resolution is highly dependent on tissue depth since the shape and the width of the beam varies along the beam direction see Figure 1.9. The lateral resolution will be best at the focal plane of the transducer [48].

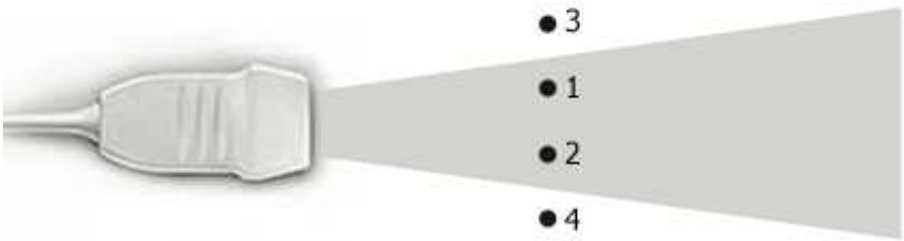

Figure 1.9. Lateral Resolution.

Reflectors labeled as 1-2 can be resolved; however, 1-3, 1-4, 2-3 and 2-4 can not be resolved.

At higher frequencies, the beam shape can be made narrower that increases transducer capability to differentiate reflectors at the same perpendicular line to the transducer. Thus, higher frequency means better lateral resolution. As mentioned for axial resolution, penetration depth decreases for increased frequency.

1.5.2. Contrast Resolution

Contrast resolution is the ability to distinguish between differences in signal intensity [49].

In photoacoustic imaging, absorption coefficient influences the signal amplitude (see Chapter 2). Tissue constituents such as lipid, water, hemoglobin, oxgenated hemoglobin have different absorption spectrums (excluding the isosbestic points) which basically generate contrast without need for external contast agents. In photoacoustic imaging, contrast resolution is determined by optical absorption.

2. THE SOLUTION OF THE PHOTOACOUSTIC EQUATION

2.1. Derivation of Photoacoustic Wave Equation

The photoacoustic wave equation can be derived by using two equations, the linear inviscid force equation and thermal expansion equation [29]

$$\rho \frac{\partial^2}{\partial t^2} \xi(\mathbf{r}, t) = -\nabla p(\mathbf{r}, t) \tag{2.1}$$

where ξ is the medium displacement and

$$\nabla \cdot \xi(\mathbf{r}, t) = -\kappa p(\mathbf{r}, t) + \beta T(\mathbf{r}, t). \tag{2.2}$$

Taking the divergence of Equation 2.1 and substituting into Equation 2.2, we get

$$\frac{\partial^2}{\partial t^2}(-\kappa \rho p(\mathbf{r}, t) + \rho \beta T(\mathbf{r}, t)) = \nabla^2 p(\mathbf{r}, t). \tag{2.3}$$

By using $V_s = \frac{1}{\sqrt{\rho\kappa}}$, the Equation 2.3 becomes

$$(\nabla^2 - \frac{1}{v_s^2}\frac{\partial^2}{\partial t^2})p(\mathbf{r},t) = -\rho\beta\frac{\partial^2}{\partial t^2}T(\mathbf{r},t). \tag{2.4}$$

By using $\rho = \frac{1}{\kappa V_s^2}$, we finally get the general photoacoustic equation that describes the photoacoustic wave generation and propagation

$$(\nabla^2 - \frac{1}{v_s^2}\frac{\partial^2}{\partial t^2})p(\mathbf{r},t) = -\frac{\beta}{\kappa v_s^2}\frac{\partial^2}{\partial t^2}T(\mathbf{r},t). \tag{2.5}$$

The left hand side of Equation 2.5 represents the wave propagation where v_S is the speed of sound, and $p(\mathbf{r},t)$ is the photoacoustic wave pressure at position $\mathbf{r}$ and time t.

The right hand side of Equation 2.5 describes the photoacoustic source where β is the thermal coefficient of volume expansion, κ is the isothermal compressibility, and $T(\mathbf{r},t)$ is the increase in temperature at position $\mathbf{r}$ and time t [29].

For a short laser pulse satisfying thermal and stress confinement condition, heat diffusion can be neglected so the following thermal equation holds

$$\rho C_v\frac{\partial T(\mathbf{r},t)}{\partial t} = H(\mathbf{r},t). \tag{2.6}$$

If we write Equation 2.6 into Equation 2.5, we get

$$(\nabla^2 - \frac{1}{v_s^2}\frac{\partial^2}{\partial t^2})p(\mathbf{r},t) = -\frac{\beta}{C_p}\frac{\partial H(\mathbf{r},t)}{\partial t} \tag{2.7}$$

where H is the heating function, the amount of heat generated by light absorption per unit volume and per unit time, ρ denotes the mass density , C_p and C_V are the specific heat capacity at constant pressure and volume, respectively [13, 29].

2.2. Solution of Photoacoustic Wave Equation for Dirac Delta Pulse Excitation

The solutions for the photoacoustic wave Equation 2.7 can be obtained by using the Green's function approach [13, 50]. Wang solved the photoacoustic equation by treating the source term as a Dirac delta function [13, 29] in time domain.

$$(\nabla^2 - \frac{1}{v_s^2}\frac{\partial^2}{\partial t^2})G(\mathbf{r}, t; \mathbf{r}^{'}, t') = -\delta(\mathbf{r} - \mathbf{r}^{'})\delta(t - t'). \tag{2.8}$$

The green function for Equation 2.8 for unbounded space is given by

$$G(\mathbf{r}, t; \mathbf{r}^{'}, t') = \frac{\delta(t - t' - \frac{|\mathbf{r}-\mathbf{r}^{'}|}{v_s})}{4\pi \mid \mathbf{r} - \mathbf{r}^{'} \mid}. \tag{2.9}$$

In this equation, $\mathbf{r}^{'}$ and $t^{'}$ stands for the source location and time. By Green's approach, the Equation 2.7 can be solved by the following expression

$$p(r, t) = \int_{-\infty}^{t^{+}} dt' \int dr' G(\mathbf{r}, t; \mathbf{r}^{'}, t')\frac{\beta}{\kappa v_s^2}\frac{\partial^2 T(\mathbf{r}^{'}, t^{'})}{\partial t^2}. \tag{2.10}$$

Writing Equation 2.9 into Equation 2.10 gives

$$p(r,t) = \frac{\beta}{4\pi\kappa v_s^2} \int dr' \frac{1}{|\mathbf{r}-\mathbf{r}'|} \frac{\partial^2 T(\mathbf{r}', t')}{\partial t^2} \tag{2.11}$$

where $t' = t - \frac{|\mathbf{r}-\mathbf{r}'|}{v_s}$.

For a short laser pulse, Equation 2.6 holds and hence Equation 2.11 becomes

$$p(r,t) = \frac{\beta}{4\pi C_p} \int dr' \frac{1}{|\mathbf{r}-\mathbf{r}'|} \frac{\partial H(\mathbf{r}', t')}{\partial t'}. \tag{2.12}$$

Substituting $t' = t - \frac{|\mathbf{r}-\mathbf{r}'|}{v_s}$ into Equation 2.12 yields

$$p(r,t) = \frac{\beta}{4\pi C_p} \frac{\partial}{\partial t} \int dr' \frac{1}{|\mathbf{r}-\mathbf{r}'|} H(r', t - \frac{|\mathbf{r}-\mathbf{r}'|}{v_s}). \tag{2.13}$$

Heating function can be decomposed into a product of radial and temporal components

$$H(r', t') = A(r')H(t') \tag{2.14}$$

where $\int H_t' dt' = 1$, then Equation 2.13 becomes

$$p(r,t) = \frac{\beta}{4\pi C_p}\frac{\partial}{\partial t}\int dr' \frac{A(r')}{|\mathbf{r}-\mathbf{r}'|} H_t(t - \frac{|\mathbf{r}-\mathbf{r}'|}{v_s}). \tag{2.15}$$

Writing $H_t(t') = \delta(t')$ yields

$$p(r,t) = \frac{\partial}{\partial t}[\frac{\beta}{4\pi C_p}\frac{1}{V_s t}\int dr' A(r')\delta(t - \frac{|\mathbf{r}-\mathbf{r}'|}{v_s})]. \tag{2.16}$$

The pressure rise just after the laser excitation can be expressed in terms of the optical absorption coefficient and the optical fluence considering the following fractional volume expansion

$$\frac{dV}{V} = -\kappa p + \beta T \tag{2.17}$$

where T is the increase in temperature.

To satisfy stress confinement condition that is laser pulse width is much shorter than the stress relaxation time, the change of the volume 2.17 can be neglected and the initial pressure rise just after the pulse can be written as [13, 29]

$$p_0(r) = \frac{\beta T(r)}{\kappa} \tag{2.18}$$

where isothermal compressibility is

$$\kappa = \frac{C_P}{\rho v_S^2 C_V}. \tag{2.19}$$

If all the absorbed electromagnetic energy is converted into heat and then non-thermal relaxation is neglected, then the increase in temperature resulted from the laser pulse can be written as

$$T = \frac{A_e(r)}{\rho C_V} \tag{2.20}$$

where $A_e(r)$ is the specific optical absorption in joules per m^3.

Combining Equation 2.18, Equation 2.19 and Equation 2.20 gives

$$A_e(r) = \frac{p_0(r)}{v_S^2}\frac{C_P}{\beta}. \tag{2.21}$$

By substituting Equation 2.21 into Equation 2.16 results in

$$p(r,t) = \frac{1}{4\pi V_s^2}\frac{\partial}{\partial t}[\frac{1}{V_s t}\int dr' p_o(r')\delta(t - \frac{|\mathbf{r} - \mathbf{r}'|}{v_s})]. \tag{2.22}$$

This equation can be used to compute photoacoustic pressure for any later time if initial pressure rise is known.

The initial pressure distribution for an optically thin slab of thickness d can be written as

$$p_0(z) = p_o U(z + \frac{d}{2}) U(-z + \frac{d}{2}) \tag{2.23}$$

where U is the Heaviside step function.

Inserting Equation 2.23 into Equation 2.22 gives

$$p(z,t) = \frac{1}{2} p_0(z - V_s t) p_0(z + V_s t). \tag{2.24}$$

For a spherical object of radius R,

$$p(r,t) = p_0[U(R - v_s t - r) + \frac{r - v_s t}{2r} U(r - |R - V_s t|) U(R + v_s t - r)]. \tag{2.25}$$

If initial pressure is

$$p_0(r) = p_o U(r) U(-r + R), \tag{2.26}$$

the final solution becomes

$$p(r,t) = \frac{r + V_s t}{2r} p_0(r + V_s t) + \frac{r - V_s t}{2r} p_0(-r + V_s t) + \frac{r - V_s t}{2r} p_0(r - V_s t). \qquad (2.27)$$

2.3. Solution of Photoacoustic Wave Equation for Gaussian Temporal Profile

In this section, the photoacoustic equation is solved in frequency domain considering the temporal part of the source term of Equation 2.7 as Gaussian. The Fourier transform approach is preferred here because Green function approach is not as straightforward as it is for dirac-delta pulse in previous section. The solution of photoacoustic equation in time domain is also obtained by using inverse Fourier transform.

The source term of photoacoustic wave Equation 2.7 is denoted by S($\mathbf{r}$,t)

$$S(\mathbf{r},t) \equiv -\frac{\beta}{C_P}\frac{\partial H(\mathbf{r},t)}{\partial t}. \tag{2.28}$$

For a Gaussian laser pulse, the temporal profile of the heating function decomposition, Equation 2.14, can be considered as the following shape

$$H(t) = \frac{e^{\frac{-t^2}{2\tau_p^2}}}{\sqrt{2\pi\tau_p^2}} \tag{2.29}$$

where τ_p is the pulse duration of the laser.

Substituting Equation 2.21 and Equation 2.29 into Equation 2.28 leads to

$$S(r,t) = -\frac{p_0(r)}{v_S^2}\frac{\partial}{\partial t}\left(\frac{e^{\frac{-t^2}{2\tau_p^2}}}{\sqrt{2\pi\tau_p^2}}\right)$$

$$= \frac{1}{\sqrt{2\pi}\tau_p^3}\frac{p_0(r)}{v_S^2}te^{\frac{-t^2}{2\tau_p^2}}. \tag{2.30}$$

Fourier transform of $S(r,t)$ yields

$$\begin{aligned}\tilde{S}(\mathbf{r},\omega) &= \frac{1}{\sqrt{2\pi}\tau_p^3}\frac{p_0(\mathbf{r})}{v_s^2}\int_{-\infty}^{\infty} t\exp(-\frac{t^2}{2\tau_p^2})\exp(i\omega t)dt \\ &= \frac{i}{\sqrt{2\pi}}\frac{p_0(\mathbf{r})}{v_s^2}\omega\exp(-\frac{\tau_p^2\omega^2}{2}).\end{aligned} \tag{2.31}$$

Using Fourier convention, $p(\mathbf{r},t) = \frac{1}{\sqrt{2\pi}}\int_{-\infty}^{\infty}\tilde{p}(\mathbf{r},\omega)\exp(-i\omega t)d\omega$, in frequency domain the photoacoustic wave Equation 2.7 can be expressed as

$$\nabla^2\tilde{p}(\mathbf{r},\omega) + \frac{\omega^2}{v_S^2}\tilde{p}(\mathbf{r},\omega) = i\frac{p_0(\mathbf{r})}{v_S^2}\omega\exp(-\frac{\tau_p^2\omega^2}{2}). \tag{2.32}$$

The Green's function of Equation 2.32 is given by the following expression [50]

$$\tilde{G}(\mathbf{r},\mathbf{r}';\omega) = -\frac{1}{4\pi \mid \mathbf{r}-\mathbf{r}^{'} \mid}\exp(i\frac{\omega}{v_s} \mid \mathbf{r}-\mathbf{r}^{'} \mid) \tag{2.33}$$

where the Green's function is an outgoing spherical wave for $\mid \mathbf{r}-\mathbf{r}^{'} \mid \rightarrow \infty$.

The solution in ω domain can be found by solving the following integral

$$\tilde{p}(r,\omega) = \int \tilde{G}(r,r';\omega)\tilde{S}(r';\omega)d^3r'. \tag{2.34}$$

Substituting Equation 2.31 and Equation 2.33 into Equation 2.34 gives

$$\tilde{p}(\mathbf{r},\omega) = -\frac{i}{4\pi}\frac{\omega}{v_S^2}\exp(-\frac{\tau_p^2\omega^2}{2})\int p_0(r')\frac{\exp(i\frac{\omega}{v_S} \mid \mathbf{r}-\mathbf{r}' \mid)}{\mid \mathbf{r}-\mathbf{r}' \mid}d^3r'. \tag{2.35}$$

For a spherical object of radius R excited by a Gaussian shaped laser beam, the initial pressure distribution can be written as [13, 29]

$$p_0(r) = p_0\theta(r)\theta(-r+R) \tag{2.36}$$

where θ is the Heaviside step function.

Writing Equation 2.36 into Equation 2.35 and taking $\mathbf{r}$ along z axis, we get

$$\begin{aligned}\tilde{p}(r,\omega) = -\frac{ip_0}{4\pi}\frac{\omega}{v_S^2}\exp(-\frac{\tau_p^2\omega^2}{2}) \\ \times\int_0^{2\pi}d\phi'\int_0^R(r')^2dr'\int_{-1}^1\frac{\exp(i\frac{\omega}{v_S} \mid \mathbf{r}-\mathbf{r}' \mid)}{\mid \mathbf{r}-\mathbf{r}' \mid}d\mu'\end{aligned} \tag{2.37}$$

where $\mu' = \cos\theta'$ and $\mid \mathbf{r}-\mathbf{r}' \mid = \sqrt{r^2+r'^2-2rr'\mu'}$.

Inserting the result of the following integral

$$\int_{-1}^{1} \frac{e^{i\frac{\omega}{v_S}\sqrt{r^2+r'^2-2rr'\mu'}}}{\sqrt{r^2+r'^2-2rr'\mu'}} d\mu' = -\frac{1}{irr'\frac{\omega}{v_S}}(e^{i\frac{\omega}{v_S}(r-r')} - e^{i\frac{\omega}{v_S}(r+r')}) \tag{2.38}$$

into Equation 2.34 gives the desired solution in ω domain

$$\tilde{p}(r,\omega) = ip_0\frac{v_S}{r}\frac{\exp(-\frac{\tau_p^2\omega^2}{2} + i\frac{\omega}{v_S}r)}{\omega^2}[\frac{\omega}{v_S}R\cos(\frac{\omega}{v_S}R) - \sin(\frac{\omega}{v_S}R)] \tag{2.39}$$

where $r > R$ or $r > r'$.

Inverse Fourier transform of $\tilde{p}(r,\omega)$ yields

$$p(\mathbf{r},t) = -\frac{i}{\sqrt{2\pi}}p_0\frac{v_S}{r}\int_{-\infty}^{\infty}\frac{e^{-\frac{\tau_p^2\omega^2}{2}+i\frac{\omega}{v_S}r-i\omega t}}{\omega^2}[\frac{\omega}{v_S}R\cos(\frac{\omega}{v_S}R) - \sin(\frac{\omega}{v_S}R)]d\omega. \tag{2.40}$$

Writing $\cos(\frac{\omega}{v_S}R)$ and $\sin(\frac{\omega}{v_S}R)$ in terms of exponentials

$$\cos(x) = \frac{e^{ix}+e^{-ix}}{2} \tag{2.41}$$

,

$$\sin(x) = \frac{e^{ix}-e^{-ix}}{2i} \tag{2.42}$$

into Equation 2.40 gives

$$p(\mathbf{r},t) = -\frac{ip_0}{2\sqrt{2\pi}}\frac{R}{r}\left[\int_{-\infty}^{\infty}\frac{e^{-\frac{\tau_p^2\omega^2}{2}+i\omega(\frac{r+R}{v_S}-t)}}{\omega}d\omega + \int_{-\infty}^{\infty}\frac{e^{-\frac{\tau_p^2\omega^2}{2}+i\omega(\frac{r-R}{v_S}-t)}}{\omega}d\omega\right]$$
$$+\frac{1}{2\sqrt{2\pi}}p_0\frac{v_S}{r}\left[\int_{-\infty}^{\infty}\frac{e^{-\frac{\tau_p^2\omega^2}{2}+i\omega(\frac{r+R}{v_S}-t)}}{\omega^2}d\omega - \int_{-\infty}^{\infty}\frac{e^{-\frac{\tau_p^2\omega^2}{2}+i\omega(\frac{r-R}{v_S}-t)}}{\omega^2}d\omega\right]. \quad (2.43)$$

The solution of photoacoustic equation can be obtained if the following I_1 and I_2 integrals are solved

$$I_1 = \int_{-\infty}^{\infty}\frac{e^{-\frac{\tau_p^2\omega^2}{2}+i\omega(\frac{r+R}{v_S}-t)}}{\omega}d\omega, \quad (2.44)$$

$$I_2 = \int_{-\infty}^{\infty}\frac{e^{-\frac{\tau_p^2\omega^2}{2}+i\omega(\frac{r+R}{v_S}-t)}}{\omega^2}d\omega. \quad (2.45)$$

These I_1 and I_2 kinds of integrals can be calculated carrying out the residue theorem [50].

To calculate the following type of integral

$$I = \int_{-\infty}^{\infty} f(z)e^{i\alpha z}dz, \quad (2.46)$$

the Jordan-Lemma has to be satisfied. Jordan-Lemma states that if $f(z) \to 0$ as $z \to \infty$, then

$$\lim_{R\to\infty}\int_{C_R} f(z)e^{i\alpha z}dz = 0 \tag{2.47}$$

where C_R is a circular path of infinite radius on the upper z plane for $\alpha > 0$. I_1 integral in complex z plane can be written as

$$\oint \frac{e^{-\frac{\tau_p^2 z^2}{2}}}{z} e^{iz(\frac{r+R}{v_S}-t)}dz = \lim_{R\to\infty}\int_{C_R} \frac{e^{-\frac{\tau_p^2 z^2}{2}}}{z} e^{iz(\frac{r+R}{v_S}-t)}dz + \int_{-\infty}^{\infty} \frac{e^{-\frac{\tau_p^2 x^2}{2}}}{x} e^{ix(\frac{r+R}{v_S}-t)}dx. \tag{2.48}$$

Here, if $(\frac{r+R}{v_S} - t) > 0$, the first integral of the right hand side of Equation 2.48 becomes zero due to the Jordan-Lemma.

Applying the residue theorem at $z = 0$ gives

$$\oint \frac{e^{-\frac{\tau_p^2 z^2}{2}}}{z} e^{iz(\frac{r+R}{v_S}-t)}dz = \begin{cases} \pi i \lim_{z\to 0}(z\frac{e^{-\frac{\tau_p^2 z^2}{2}}}{z} e^{iz(\frac{r+R}{v_S}-t)}) & if\ (\frac{r+R}{v_S} - t) > 0, \\ -\pi i \lim_{z\to 0}(z\frac{e^{-\frac{\tau_p^2 z^2}{2}}}{z} e^{iz(\frac{r+R}{v_S}-t)}) & if\ (\frac{r+R}{v_S} - t) < 0. \end{cases} \tag{2.49}$$

Hence,

$$I_1 = \pi i \,\mathrm{sgn}(\frac{r+R}{v_S} - t) \tag{2.50}$$

where $\mathrm{sgn}(x)$ is the signum function. Following the similar steps, I_2 integral can also be calculated taking into consideration that $z = 0$ is a second order pole

$$I_2 = -\pi(\frac{r+R}{v_S} - t)\,\mathrm{sgn}(\frac{r+R}{v_S} - t). \tag{2.51}$$

Substituting Equation 2.50 and Equation 2.51 into Equation 2.43 leads to the following solution of photoacoustic equation in time domain for a spherical object homogeneously heated by a short laser pulse having a Gaussian temporal profile

$$\begin{aligned} p(r,t) = \frac{1}{2}\sqrt{\frac{\pi}{2}}\frac{p_0}{r}[(r - v_s t)\ \mathrm{sgn}(\frac{r+R}{v_s} - t) \\ +(-r + v_s t)\ \mathrm{sgn}(\frac{r-R}{v_s} - t)]. \end{aligned} \tag{2.52}$$

If a pulsed laser is sent to a spherical object of radius R, the object is heated and an initial pressure p_0 is created inside the object. There are three cases based on the propagation time when observation point is outside the spherical object [29]. If $r - R > v_S t$, the spherical object does not intersect with the spherical shell of radius $v_S t$ which is centered at the observation point so that $p(r,t)$ becomes zero. If $v_S t$ is between the interval [r-R, r+R], the heated spherical object touches the spherical shell of radius $v_S t$. Pressure can be described by Equation 2.52. If $r + R < v_S t$, then the spherical object cannot intersect with the spherical shell. For this reason, $p(r,t)$ becomes zero.

Therefore, these three cases can be combined into the following equation by utilizing the Heaviside step function, $\theta(x)$,

$$\begin{aligned} p(r,t) = \frac{1}{2}\sqrt{\frac{\pi}{2}}\frac{p_0}{r}\{(r - v_s t)\ \mathrm{sgn}(\frac{r+R}{v_s} - t) \\ +(-r + v_s t)\ \mathrm{sgn}(\frac{r-R}{v_s} - t)\} \\ \times\theta(r - \mid R - v_s t \mid)\theta(-r + R + v_s t) \end{aligned} \tag{2.53}$$

for outside the object ($r > R$).

Substituting Equation 2.20 into Equation 2.18 leads to

$$p_0 = \frac{\beta}{\kappa\rho C_V} A_e. \tag{2.54}$$

Defining Grueneisen parameter $\Gamma = \frac{\beta}{\kappa\rho C_V}$ and writing $A_e = \mu_a F$, Equation 2.54 becomes

$$p_0 = \Gamma\mu_a F \tag{2.55}$$

where μ_a and F stand for the optical absorption coefficient and the optical fluence, respectively.

Hence, the photoacoustic wave can be expressed in terms of the parameters of the spherical object

$$p(r,t) = \frac{1}{2}\sqrt{\frac{\pi}{2}}\frac{\Gamma\eta_{th}\mu_a F}{r}\{(r - v_s t)\ \mathrm{sgn}(\frac{r+R}{v_s} - t) + (-r + v_s t)\ \mathrm{sgn}(\frac{r-R}{v_s} - t)\} \times\theta(r - \mid R - v_s t \mid)\theta(-r + R + v_s t). \tag{2.56}$$

The photoacoustic signals can be detected if an ultrasonic transducer is located outside the spherical object. Thus, the optical absorption coefficient μ_a can be calculated by inserting the detected signal and the other parameters in Equation 2.56.

In Figure 2.1, the normalized photoacoustic pressure waves as a function of normalized time are plotted for different radial locations. Laser pulse results in an initial pressure p_0 via thermal expansion. This initial pressure is constant throughout the spherical object. Each spherical pressure wave is split into two waves which have the same amplitude. In Figure 2.1, diverging spherical wave travels outward which is on the positive y axis whereas converging spherical wave travels inwards which is on the negative y axis. These results are in good accordance with the literature [13, 51]. It is clearly observed that, photoacoustic signal is proportional to absorption coefficient and the fluence.

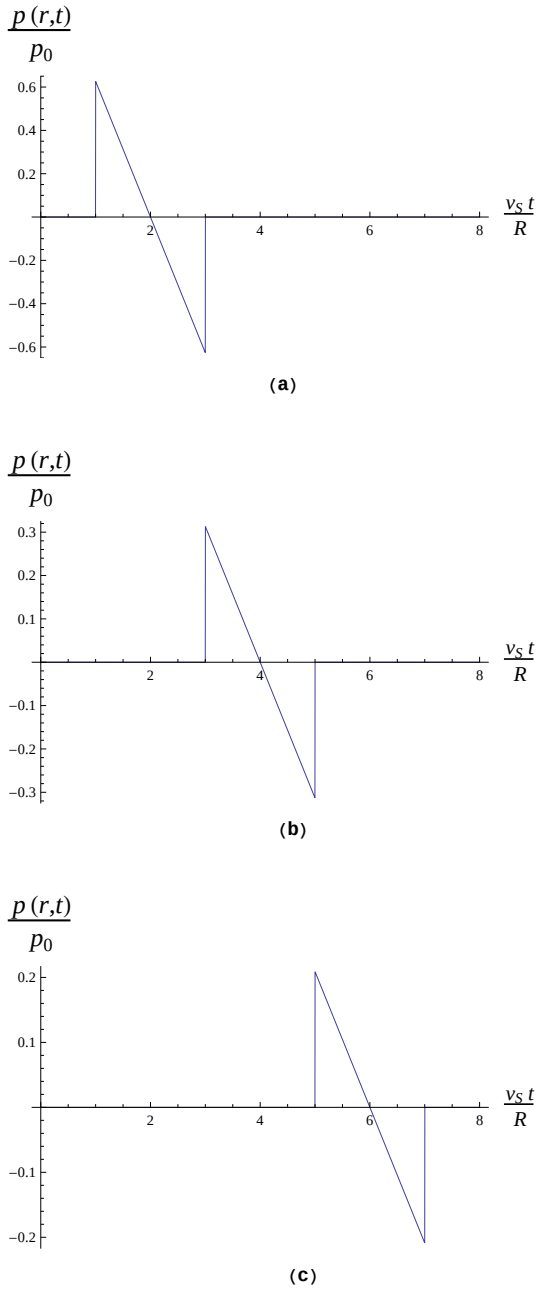

Figure 2.1. Normalized photoacoustic pressure waves generated inside a spherical object excited by a short laser pulse for a Gaussian temporal profile vs. normalized time observed at different radial positions (a) r=2 R (b) r=4 R (c) r=6 R.

2.4. Solution of Photoacoustic Equation for Gaussian Spatiotemporal Profile

In this section, we treat the radial part of the source term of the photoacoustic equation as a Gaussian profile which is more realistic compared to the uniform radial profile case.

$$p_0(r) = p_0 e^{-\frac{r^2}{2\tau^2}} \theta(r)\theta(-r+R) \tag{2.57}$$

where τ is the beam width of the laser.

Fourier transform of $p(r,t)$ gives

$$\tilde{p}(r,\omega) = -\frac{p_0}{2\pi}\frac{1}{v_S r} e^{-\frac{\tau_p^2\omega^2}{2}} [\int_0^R r' e^{-\frac{r'^2}{2\tau^2}} (e^{i\frac{\omega}{v_S}(r-r')} - e^{i\frac{\omega}{v_S}(r+r')}) dr'. \tag{2.58}$$

The solution of the photoacoustic equation in time domain can be obtained by calculating the following integral

$$p(r,t) = -\frac{p_0}{2\sqrt{2\pi}}\frac{1}{v_S r}\int_0^R r' e^{-\frac{r'^2}{2\tau^2}} \int_{-\infty}^{\infty} (e^{-\frac{\tau_p^2\omega^2}{2} + i\omega(\frac{r-r'}{v_S} - t)} - e^{-\frac{\tau_p^2\omega^2}{2} + i\omega(\frac{r+r'}{v_S} - t)}) d\omega dr' \tag{2.59}$$

Substituting

$$\int_{-\infty}^{\infty} e^{-\frac{\tau_p^2\omega^2}{2} + i\omega(\frac{r-r'}{v_S} - t)} d\omega = \frac{\sqrt{2\pi}}{\tau_p} e^{-\frac{(\frac{r-r'}{v_S} - t)^2}{2\tau_p^2}} \tag{2.60}$$

into Equation 2.59 leads to

$$p(r,t) = -\frac{p_0}{2}\frac{1}{v_S r \tau_p}\int_0^R r'(e^{-\frac{r'^2}{2\tau^2}-\frac{(\frac{r-r'}{v_S}-t)^2}{2\tau_p^2}} - e^{-\frac{r'^2}{2\tau^2}-\frac{(\frac{r+r'}{v_S}-t)^2}{2\tau_p^2}})dr' \tag{2.61}$$

for outside the object ($r > R$). Calculations of J_1 and J_2 integrals on the right hand side of Equation 2.61

$$J_{1,2} = \int_0^R r' \exp[-\frac{r'^2}{2\tau^2} - \frac{(\frac{r\mp r'}{v_s}-t)^2}{2\tau_p^2}]dr' \tag{2.62}$$

give the following results

$$\begin{aligned} J_1 &= \int_0^R r' \exp[-\frac{r'^2}{2\tau^2} - \frac{(\frac{r-r'}{v_s}-t)^2}{2\tau_p^2}]dr' \qquad (2.63)\\ &= \frac{\tau_p \tau^2 v_s}{2(\tau^2+\tau_p^2 v_s^2)^{3/2}} \exp[-\frac{(r-v_s t)^2}{2\tau_p^2 v_s^2}] \\ &\times\{\sqrt{2\pi}\tau(r-v_s t)\exp[\frac{\tau^2(r-v_s t)^2}{2\tau_p^2 v_s^2(\tau^2+\tau_p^2 v_s^2)}] \\ &\times[\mathrm{erf}[\frac{\tau^2(-r+R+v_s t)+R\tau_p^2 v_s^2}{\sqrt{2}\tau_p \tau v_s\sqrt{\tau^2+\tau_p^2 v_s^2}}] + \mathrm{erf}[\frac{\tau(r-v_s t)}{\sqrt{2}\tau_p v_s\sqrt{\tau^2+\tau_p^2 v_s^2}}]] \\ &-2\tau_p v_s\sqrt{\tau^2+\tau_p^2 v_s^2}[\exp[\frac{1}{2}R(-\frac{-2r+R+2v_s t}{\tau_p^2 v_s^2} - \frac{R}{\tau^2})] - 1] \qquad (2.64) \end{aligned}$$

and

$$\begin{aligned} J_2 &= \int_0^R r' \exp[-\frac{r'^2}{2\tau^2} - \frac{(\frac{r+r'}{v_s}-t)^2}{2\tau_p^2}]dr' \\ &= \frac{\tau_p \tau^2 v_s}{2(\tau^2+\tau_p^2 v_s^2)^{3/2}} \exp[-\frac{(r+R-v_s t)^2}{2\tau_p^2 v_s^2} - \frac{R^2}{2\tau^2}] \end{aligned}$$

$$\times\{\sqrt{2\pi}\tau(r-v_st)\exp[\frac{(\tau^2(r+R-v_st)+R\tau_p^2v_s^2)^2}{2\tau_p^2\tau^2v_s^2(\tau^2+\tau_p^2v_s^2)}]$$
$$\times[\mathrm{erf}[\frac{\tau(r-v_st)}{\sqrt{2}\tau_pv_s\sqrt{\tau^2+\tau_p^2v_s^2}}]-\mathrm{erf}[\frac{\tau^2(r+R-v_st)+R\tau_p^2v_s^2}{\sqrt{2}\tau_p\tau v_s\sqrt{\tau^2+\tau_p^2v_s^2}}]]$$
$$+2\tau_pv_s\sqrt{\tau^2+\tau_p^2v_s^2}[\exp[\frac{R(2(r-v_st)+\frac{R\tau_p^2v_s^2}{\tau^2}+R)}{2\tau_p^2v_s^2}]-1]\}, \tag{2.65}$$

respectively where $\mathrm{erf}(x)$ is the error function.

Therefore, substituting the integrals J_1 and J_2 into Equation 2.61 gives

$$p(r,t)=\frac{p_0\tau^2}{4r(\tau^2+\tau_p^2v_s^2)^{3/2}}\exp[-\frac{2R(r-v_st)+2(r-v_st)^2+R^2}{2\tau_p^2v_s^2}-\frac{R^2}{2\tau^2}]$$
$$\times\{\sqrt{2\pi}\tau(r-v_st)[\mathrm{erf}[\frac{\tau^2(-r+R+v_st)+R\tau_p^2v_s^2}{\sqrt{2}\tau_p\tau v_s\sqrt{\tau^2+\tau_p^2v_s^2}}]$$
$$\times\exp[\frac{(r+R-v_st)^2}{2\tau_p^2v_s^2}+\frac{\tau^2(r-v_st)^2}{2\tau_p^2v_s^2(\tau^2+\tau_p^2v_s^2)}+\frac{R^2}{2\tau^2}]$$
$$+\mathrm{erf}[\frac{\tau^2(r+R-v_st)+R\tau_p^2v_s^2}{\sqrt{2}\tau_p\tau v_s\sqrt{\tau^2+\tau_p^2v_s^2}}]$$
$$\times\exp[\frac{\frac{(\tau^2(r+R-v_st)+R\tau_p^2v_s^2)^2}{\tau^2(\tau^2+\tau_p^2v_s^2)}+(r-v_st)^2}{2\tau_p^2v_s^2}]]$$
$$-2\tau_pv_s\sqrt{\tau^2+\tau_p^2v_s^2}\exp[\frac{(r-v_st)^2}{2\tau_p^2v_s^2}][\exp[\frac{2R(r-v_st)}{\tau_p^2v_s^2}]-1]\}. \tag{2.66}$$

When the three cases based on the propagation time mentioned in the previous section are considered, for outside the spherical object, the photoacoustic pressure wave takes its final form:

$$p(r,t)=\frac{p_0\tau^2}{4r(\tau^2+\tau_p^2v_s^2)^{3/2}}\exp[-\frac{2R(r-v_st)+2(r-v_st)^2+R^2}{2\tau_p^2v_s^2}-\frac{R^2}{2\tau^2}]$$

$$\times\{\sqrt{2\pi}\tau(r-v_st)[\mathrm{erf}[\frac{\tau^2(-r+R+v_st)+R\tau_p^2v_s^2}{\sqrt{2}\tau_p\tau v_s\sqrt{\tau^2+\tau_p^2v_s^2}}]$$
$$\times\exp[\frac{(r+R-v_st)^2}{2\tau_p^2v_s^2}+\frac{\tau^2(r-v_st)^2}{2\tau_p^2v_s^2(\tau^2+\tau_p^2v_s^2)}+\frac{R^2}{2\tau^2}]$$
$$+\mathrm{erf}[\frac{\tau^2(r+R-v_st)+R\tau_p^2v_s^2}{\sqrt{2}\tau_p\tau v_s\sqrt{\tau^2+\tau_p^2v_s^2}}]$$
$$\times\exp[\frac{\frac{(\tau^2(r+R-v_st)+R\tau_p^2v_s^2)^2}{\tau^2(\tau^2+\tau_p^2v_s^2)}+(r-v_st)^2}{2\tau_p^2v_s^2}]]$$
$$-2\tau_pv_s\sqrt{\tau^2+\tau_p^2v_s^2}\exp[\frac{(r-v_st)^2}{2\tau_p^2v_s^2}][\exp[\frac{2R(r-v_st)}{\tau_p^2v_s^2}]-1]\}$$
$$\times\theta(r-\mid R-v_st\mid)\theta(-r+R+v_st). \qquad (2.67)$$

If $p_0=\Gamma\mu_aF$ is written into Equation 2.67 in order to relate the spherical object's parameters to the signal, the following expression is obtained

$$p(r,t)=\frac{\Gamma\eta_{th}\mu_aF\tau^2}{4r(\tau^2+\tau_p^2v_s^2)^{3/2}}$$
$$\times\exp[-\frac{2R(r-v_st)+2(r-v_st)^2+R^2}{2\tau_p^2v_s^2}-\frac{R^2}{2\tau^2}]$$
$$\times\{\sqrt{2\pi}\tau(r-v_st)[\mathrm{erf}[\frac{\tau^2(-r+R+v_st)+R\tau_p^2v_s^2}{\sqrt{2}\tau_p\tau v_s\sqrt{\tau^2+\tau_p^2v_s^2}}]$$
$$\times\exp[\frac{(r+R-v_st)^2}{2\tau_p^2v_s^2}+\frac{\tau^2(r-v_st)^2}{2\tau_p^2v_s^2(\tau^2+\tau_p^2v_s^2)}+\frac{R^2}{2\tau^2}]$$
$$+\mathrm{erf}[\frac{\tau^2(r+R-v_st)+R\tau_p^2v_s^2}{\sqrt{2}\tau_p\tau v_s\sqrt{\tau^2+\tau_p^2v_s^2}}]$$
$$\times\exp[\frac{\frac{(\tau^2(r+R-v_st)+R\tau_p^2v_s^2)^2}{\tau^2(\tau^2+\tau_p^2v_s^2)}+(r-v_st)^2}{2\tau_p^2v_s^2}]]$$
$$-2\tau_pv_s\sqrt{\tau^2+\tau_p^2v_s^2}\exp[\frac{(r-v_st)^2}{2\tau_p^2v_s^2}][\exp[\frac{2R(r-v_st)}{\tau_p^2v_s^2}]-1]\}$$
$$\times\theta(r-\mid R-v_st\mid)\theta(-r+R+v_st). \qquad (2.68)$$

Hence, Equation 2.68 gives the photoacoustic pressure wave resulted from a short

laser pulse which has both Gaussian temporal and radial profiles.

For biomedical optics applications, we take realistic values of $v_S = 1480\, m/s$, $\tau_p = 6.5\, ns$, $R = 3\, mm$ from references [13,20]. In Figure 2.2 and Figure 2.3, we observe the change of the normalized photoacoustic wave $\frac{p(r,t)}{p_0}$ as a function the normalized time $\frac{v_S t}{R}$ for $\frac{R}{\tau} = 1 - 10$ values using Equation 2.67. In Figure 2.3, the photoacoustic wave has a different shape rather than a linear form when τ becomes comparable with the size of the spherical object, R.

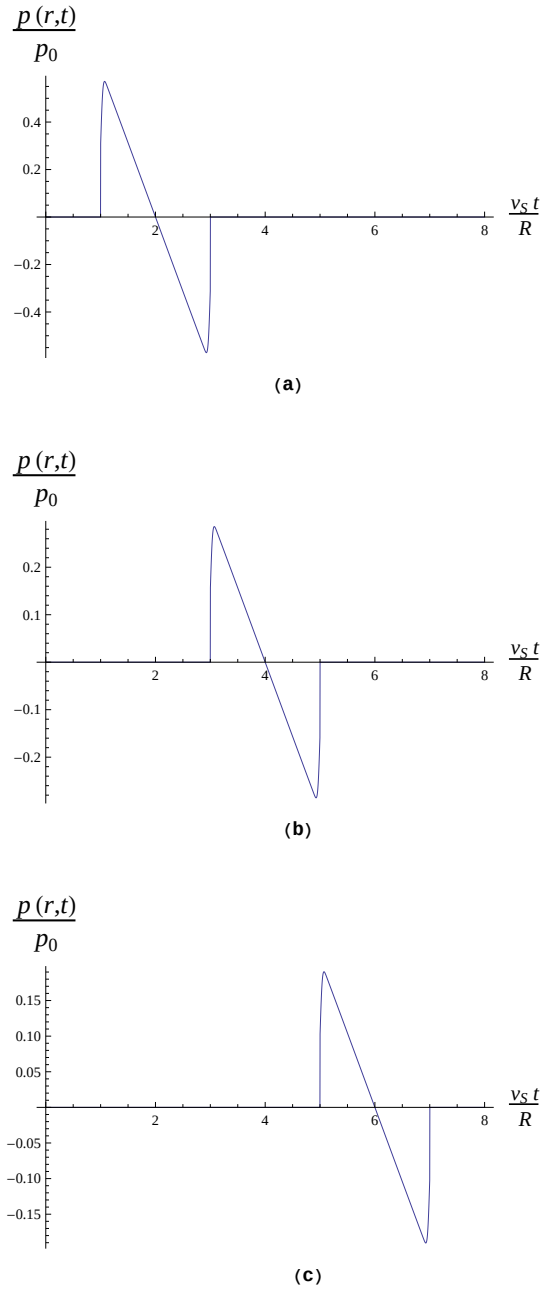

Figure 2.2. Normalized pressure wave $\frac{p(r,t)}{p_0}$ vs. normalized time $\frac{v_S t}{R}$ for (a) $r = 2R$ (b) $r = 4R$ (c) $r = 6R$ where $\frac{\tau}{R} = \frac{1}{10}$.

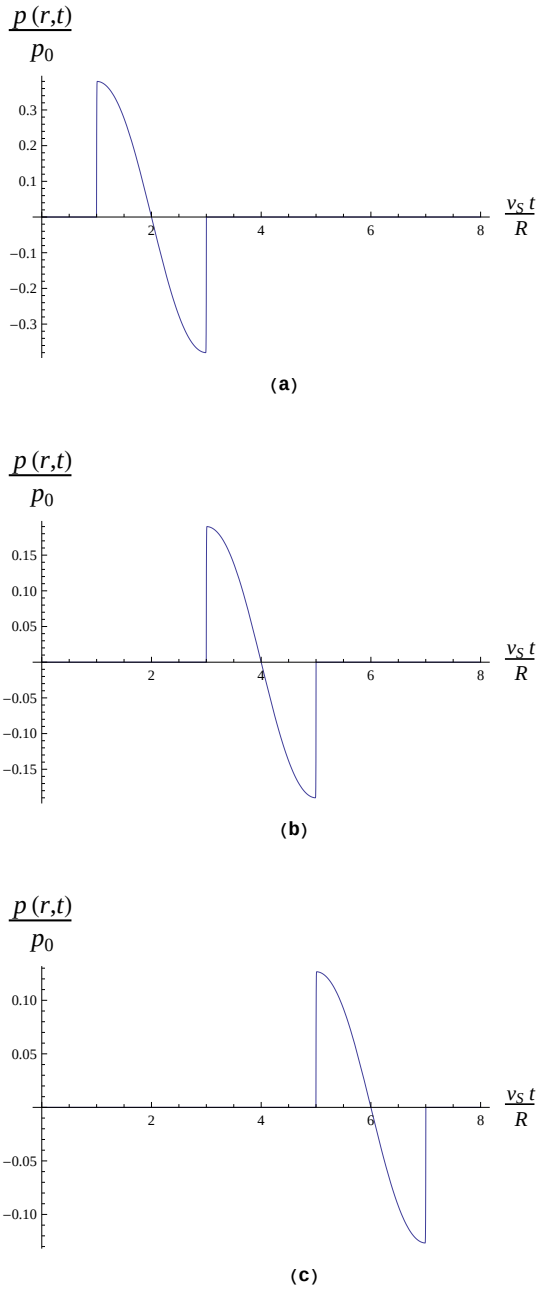

Figure 2.3. Normalized pressure wave $\frac{p(r,t)}{p_0}$ vs. normalized time $\frac{v_S t}{R}$ for (a) $r = 2R$ (b) $r = 4R$ (c) $r = 6R$ where $\frac{\tau}{R} = 1$.

In Figure 2.4, using Equation 2.68, the change of the normalized pressure waves are observed with the increasing pulse duration τ_p at $t = 5\ \mu s$ for various τ, the standard deviation of the radial profile, values.

Pulse energy of a laser is

$$E = P_{peak}\tau_p, \tag{2.69}$$

where E and P_{peak} are energy and peak power of the laser, respectively.

Figure 2.4 shows that the photoacoustic wave is a decreasing function of the pulse duration because according to Equation 2.69 the pulse duration is inversely proportional to peak power of the laser provided that the energy of laser . For a particular wavelength, i.e., constant absorption coefficient, the amplitude of PA signal decreases with increased pulse duration for constant pulse energy. In addition to this, when the pulse duration gets a larger value than the acoustic confinement time or the thermal confinement time, then the photoacoustic Equation 2.7 is no longer valid for such a large pulse duration value. The other way round, shorter pulse duration yields bigger photoacoustic wave amplitude. This condition holds as long as pulse duration allows light to be only linearly absorbed. For durations around picoseconds or femtoseconds, thermal and photoacoustic effects diminishes, intensity dependent non-linear laser tissue interactions occurs. As a non-linear effect, e.g., two photon absorption cause tissue damage.

Figure 2.4 also shows that as $\frac{R}{\tau}$ increases, the change of the normalized signal decreases slightly because the radial profile becomes very sharp and behaves like a Dirac delta function so that the laser parameters (pulse duration and beam width) begin to lose their effects on the signal.

Average power of the laser is given by

$$P_{avg} = E.PRF, \tag{2.70}$$

where P_{avg}, E, and PRF stand for the average power, the energy, and the repetition frequency, respectively. When the average power of the laser is constant, decreasing pulse repetition frequency results in an increase in the energy according to Equation 2.70 so that the amplitude of the signal increases since the photoacoustic wave is proportional to the fluence and hence the energy of the laser from Equation 2.68. It should also taken into consideration that the decrease in PRF results in slow data aquisition speed.

In Figure 2.5, the effect of the average power of the laser on the signal is also examined. Figure 2.5 confirms the previous results. The signal is a increasing function of the peak power.

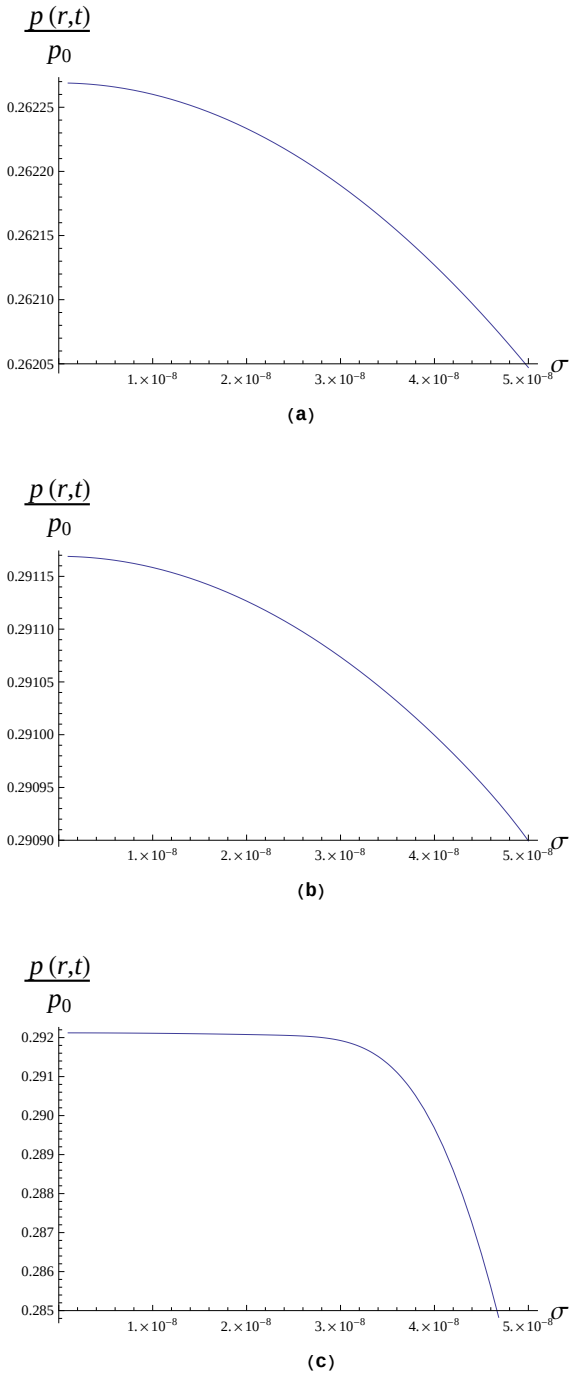

Figure 2.4. Normalized pressure wave $\frac{p(r,t)}{p_0}$ vs. pulse duration τ_p at $t = 5\,\mu s$ for (a) $\frac{R}{\tau} = 1$ (b) $\frac{R}{\tau} = 5$ (c) $\frac{R}{\tau} = 10$ where $\frac{r}{R} = 2$.

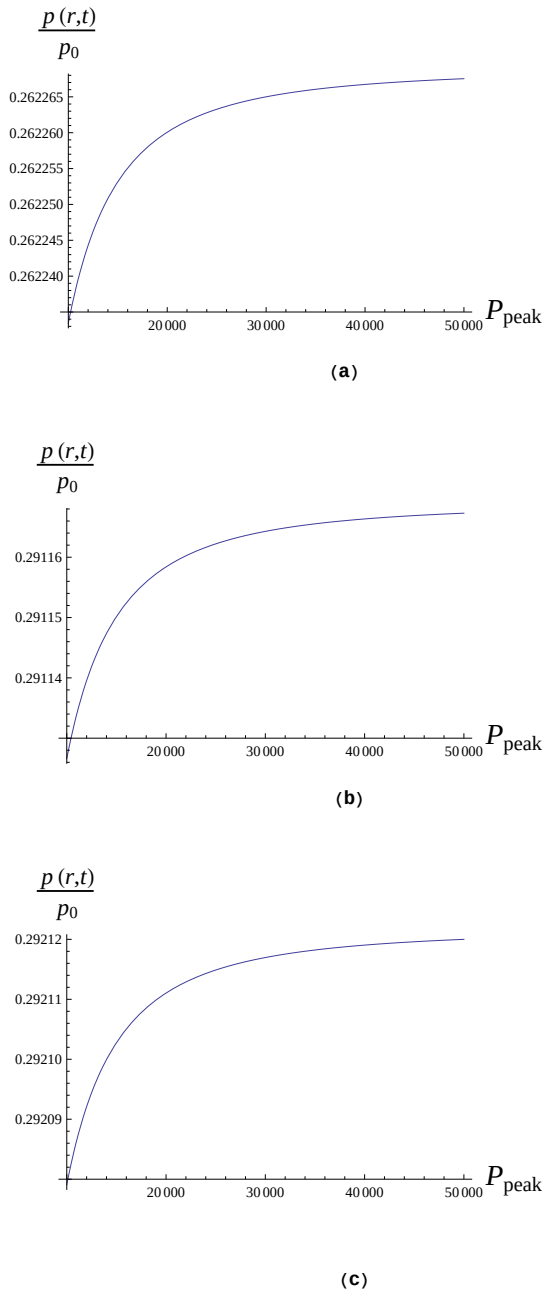

Figure 2.5. Normalized pressure wave $\frac{p(r,t)}{p_0}$ vs. P_{peak} at $t = 5\ \mu s$ for (a) $\frac{R}{\tau} = 1$ (b) $\frac{R}{\tau} = 5$ (c) $\frac{R}{\tau} = 10$ where $\frac{r}{R} = 2$ and E=0.2 mJ.

3. DESIGN OF FIBER LASER FOR PHOTOACOUSTIC IMAGING

3.1. Purpose

Photoacoustic Microscopy (PAM) research, as an imaging modality, has shown promising results in, imaging angiogenesis and cutaneous malignancies like melanoma, revealing systemic diseases including diabetes, hypertension, coronery artery, cardiovascular disease from their effect on the microvasculature, tracing drug efficiency and assessment of therapy, monitoring healing processes such as wound cicatrization, brain imaging and mapping, neuroscientific evaluations as mentioned in Chapter 1 under the subsection of applications of photoacoustic imaging. In malignant tumor, the growth of new blood vessels from pre-existing vessels, angiogenesis, increased the importance of imaging microvasculature by means of photoacoustic imaging. Clinically, PAM can be used as a diagnostic and predictive medicine tool; even have a part in preventing of diseases.

Pulse duration, pulse energy and PRF (pulse repetition frequency) of laser used in PAM affect signal amplitude and quality, data acquisition speed and indirectly the spatial resolution; thus, significant to monitor above-mentioned diseases and alterations. Current lasers used in photoacoustic imaging are commercially available Q-switched lasers, low-power laser diodes or fiber lasers with non-adjustable properties. The ready-made lasers bring about some systematic limitations on current microscopy systems. Acquisition time is long, wavelength and energy are non adjustable. Microvasculature and cellular imaging require different properties of lasers. In order to eradicate constraints, we built a fiber laser in collaboration with Ultrafast Optics and Lasers Group of Bilkent University specifically for photoacoustic microscopy.

3.2. Lasers Used for Photoacoustic Imaging

Photoacoustic imaging is not a new concept and lasers have used in this kind of imaging since 2000s. However, using fiber lasers in photoacoustic imaging is something new and there are just a few researches made about photoacoustic microscopy using these lasers.

In 2012, Zhang *et al.* [52] used two different lasers for imaging myocardial sheet architecture of a mouse. For spectral measurement, they used an integrated diode-pumped Q-switched Nd:YAG laser with a tunable wavelength between 210 to 2600 nm. However, the repetition rate of the laser is 1 kHz which is insufficient for fast imaging; thus, they also used a Nd: YVO4 laser with a fixed wavelength of 532nm providing 50 kHz repetition rate. Fast repetition rate and adjustable wavelength are required for better imaging. The left ventricular wall area was imaged by PAM with $\sim$ 50 nJ pulse energy and a saline-perfused blood-free heart of a mouse imaged by $\sim$ 80 nJ pulse energy which is comparatively low. In Chapter 2, it is theoretically derived and showed that when the pulse energy increases, the amplitude of the signal also increases which improves the quality of image as long as the fluence is in ANSI (American National Standards Institute) safety limits.

Also in 2012, Yeh *et al.* [53] used two lasers, one solid state laser and a wavelength-tunable laser for imaging blood pulse wave. The mouse ear is exposed to dual wavelength, 532 nm from the solid state laser and 563 nm from the wavelength tunable laser in order to study the differential responses of arteries and veins to cardiac pulsation. Oxygenated hemoglobin is dominant in the arteries whereas de-oxygenated hemoglobin overwhelms the veins. The absorption spectrum of oxygenated and de-oxygenated hemoglobin has peaks at different wavelengths which necessitates multi-wavelength exposure for imaging arteries and veins at the same time. The Figure 3.2 show the absorption spectrum of oxygenated and de-oxygenated hemoglobin around 500 nm.

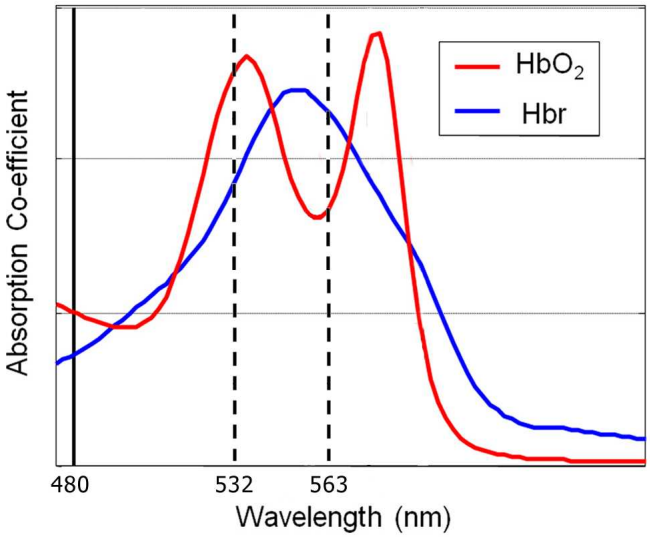

Figure 3.1. Absorption Spectrum of Hemoglobin and Oxygenated Hemoglobin around 500 nm [54].

In 2011, Krumholz *et al.* [32] used Nd:YLF pumped dye laser in order to perform two experiments, an ex vivo study to characterize the signal from tyrosinase-catalyzed melanin, and an in vivo experiment to show the capability to spectrally separate melanin from blood. Four different tubes including lysed oxygenated blood, melanoma cells, embriyonic kidney cells contains tyrosinase gene that induces melanin and embriyonic kidney cells overexpressing the tyrosinase gene are exposed to three different wavelengths, 584, 590 and 600 nm once at a time. Absorption by blood decreased significantly when compared to absorption by melanin with increasing wavelength. This difference was sufficient to distinguish blood from melanin. After filtering, the incident energy was around 100 nJ and the repetition rate of laser was not fast enough to get real time imaging.

In 2011, Favazza *et al.* [55] used two different wavelengths: 561 nm and 570 nm for functional imaging of cutaneous microvasculature in human skin. The first wavelength, 561 nm is the local maximum of de-oxygenated hemoglobin and the second one, 570 nm is an isosbestic wavelength for oxygenated and de-oxygenated hemoglobin so that the changes in the MAPs collected at these particular wavelengths can show the relative increase or decrease in de-oxygenated hemoglobin concentration. Table 3.1 shows characteristics of Q-Switched lasers that are used in recent researches.

Table 3.1. Characteristics of Q-Switched lasers and central frequency (CF) of transducers that are used in recent researches [32, 52–61].

	Laser	τ_p (ns)	Fluence/ Energy	PRF	Wavelength (nm)	CF (MHz)
Yang *et al.* (2012)	Nd:YAG	8-10	40 nJ	10 Hz	532, 680-960	22
Zhang *et al.* (2012)	Nd:YAG Nd: YVO4	N/A	80 nJ	1 kHz 50 kHz	210 to 2600 532	40
Yeh *et al.* (2012)	Nd:YAG Nd:YAG	N/A	N/A	N/A	532, 563	50
Krumholz *et al.* (2011)	Nd:YLF	N/A	0.1 μJ	N/A	584, 590, 600	75
Favazza *et al.* (2011)	Nd:YLF	5	2 mJ/cm^2	1 kHz	561, 570	20
Yao et al. (2011)	Nd:YLF	N/A	0.1 μJ	N/A	523	N/A
J.Jo and X.Yang (2011)	Nd:YAG	N/A	20 mJ/cm^2	N/A	680, 797	5
M.Liu and T.Buma (2010)	Nd:YAG	0.6	8 μJ	6.6 kHz	570-930	25
L.D Liao and M.L.Li (2010)	Nd:YAG	4	6 mJ/cm^2	10 Hz	560, 570, 600	25
Staley *et al.* (2010)	Nd:YAG	N/A	N/A	10 Hz	764	25

In 2011, Wang *et al.* [62] also used a fiber laser with a wavelength of 1064 nm for melanoma cell detection. The laser has a 10-ns pulse width and a repetition rate of 50 kHz. Melanin is a broadband absorber; thus, the laser can be used for melanoma detection but the optical absorption of hemoglobin at 1064 nm is comparatively low; thus, the laser cannot exploit from absorption peaks of hemoglobin, oxygenated hemoglobin and de-oxygenated hemoglobin.

In 2011, Shi *et al.* [63] used diode-pumped nanosecond-pulsed ytterbium-doped 532 nm fiber laser with pulse repetition rate up to 600 kHz in photoacoustic microscope. By means of high repetition rate, they achieved near real time imaging. Furthermore, optical absorption of hemoglobin at 532-nm is also high. The system is advanced in many ways when compared to solid state lasers such that it is two orders of magnitude faster than conventional system without compromising lateral resolution. The main disadvantage of the system is its fixed wavelength since variety of wavelengths could be used in applications such as the study of oxygen heterogeneity in tumors and other tissue abnormalities revealed by the changes in the oxygenated hemoglobin. Table 3.2 shows characteristics of Q-Switched lasers that are used in recent researches.

Table 3.2. Characteristics of fiber lasers and central frequency (CF) of transducers that are used in recent researches [62–64].

	Laser	τ_p (ns)	Fluence/ Energy	PRF	Wavelength (nm)	CF (MHz)
Shao *et al.* (2012)	Yd-Doped Mode-Locked	1	20 μJ	Up to 600 kHz	532	3.5
Wang *et al.* (2011)	N/A	10	0.92 μJ	50 kHz	1064	40
Shi *et al.* (2011)	Yd-Doped Mode-Locked	1	20 μJ	Up to 600 kHz	532	50

As a former study, in 2005, Allen *et al.* [26] used laser diodes for photoacoustic imaging. Their research has shown that detectable signals can be generated in superficial blood vessel to monitor blood oxygenation and volume. Taking advantage of pulse duration tunability of laser diodes, they used various pulse durations between 10 ns to 200 ns in order to examine the effect of the pulse length of the laser. However, the energy of laser diode is low compared to a typical Q-switched laser, signal averaging is

required for laser diodes. Their study showed that with signal averaging over second, the signal to noise ratio produced by a 10 mJ Q-switched laser pulse would be 22.3 times greater than of the laser diode. Combining 12 laser diodes would provide a SNR (Signal to noise ratio) equivalent to a 10 mJ Q-switched laser pulse. Therefore, by combining a reasonable number of laser diodes, it should be possible to obtain adequate SNR for NIR spectroscopic photoacoustic applications. Table 3.3 shows characteristics of Q-Switched lasers that are used in recent researches.

Table 3.3. Characteristics of fiber lasers and central frequency (CF) of transducers that are used in recent researches [26, 65].

	Laser	τ_p (ns)	Fluence/ Energy	PRF	Wavelength (nm)	CF (MHz)
Zeng *et al.* (2012)	Laser Diode	100	5.6 μJ	0.8 kHz	905	10
Allen *et al.* (2005)	Pulsed Laser Diode	10 to 200	N/A	N/A	940	N/A

3.3. Fiber Laser Set- Up

3.3.1. Oscillator

The oscillator consists of a 0.7 m long Yb-doped fiber, followed by a 70% coupler, an 8 nm bandpass filter, an inline isolator to ensure unidirectional operation, an output coupler of 10%, two polarization controllers, a 50 m long HI-1060 single mode fiber for Sagnac loop, and 2x2 40% coupler for NOLM (non linear optical loop mirror) [66]. Although the oscillator can operate without the bandpass filter, it adjusts the central wavelength and improves stability. As a pump source, a fiber-coupled single-mode 980-nm diode laser delivering a maximum power of 650 mW is used. Pump-protection filter rejects unwanted backward propagating light within the fiber, if any, because backward power can cause laser diode to break down. The fundamental repetition rate of the cavity is 3.1 MHz. Polarization controllers are used manually in order to assist mode-locked operation of the laser. Part of the output is split with a 10% fiber which seeds the amplification stage with oscillations of 24 mW power and 8 nJ energy. Figure 3.2 shows the schematics of the oscillator setup.

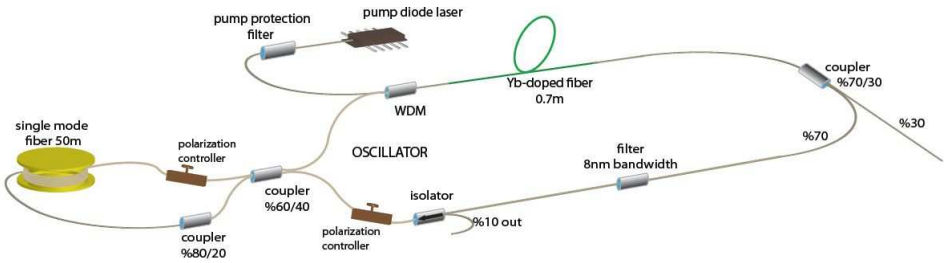

Figure 3.2. Schematic of the Oscillator Setup. WDM: Wavelength-division multiplexer.

3.3.2. Pre-Amplifier

Pre-amplifier comprises of 1.0 m long Yd doped fiber followed by fiber-integrated acousto-optic modulator (AOM) that is connected to FPGA (field programmable gate array) circuit. Fiber-coupled single-mode 980 nm diode laser delivering a maximum power of 650 mW is used as pump source. The acousto-optic modulator (AOM) allows the frequency, intensity and direction of a laser beam to be modified. A piezoelectric transducer is attached to piece of glass through which the light propagates. The light experiences Bragg diffraction due to refractive index grating generated by the sound wave traveling through the crystal. The frequency and direction of the scattered beam can be controlled by means of the frequency of the sound wave; thus, the desired pulse burst mode can be impressed. The optical power can also be controlled by the acoustic power. As long as the acoustic power is sufficiently high, more than 50% of the optical power and in some cases even more than 95% can be diffracted [67]. The amplifier levels the signal up to 300 mW power that corresponds to 100 nJ energy. By means of AOM, the repetition rate is reduced to 100 kHz which also results in optical power loss. Complete control over the pulse train, including generation of non-uniform pulse trains, is achieved via the AOM through custom-developed field-programmable gate-array (FPGA) electronics explained below. Another amplifier including 980 nm diode laser delivering a maximum power of 650 mW and 1.0 m long Yd doped fiber is built in order to compensate for decreased optical power and average power is increased to 150 mW that corresponds to 1.5 μJ pulse energy. Figure 3.3 shows the schematics of the pre-amlifier setup.

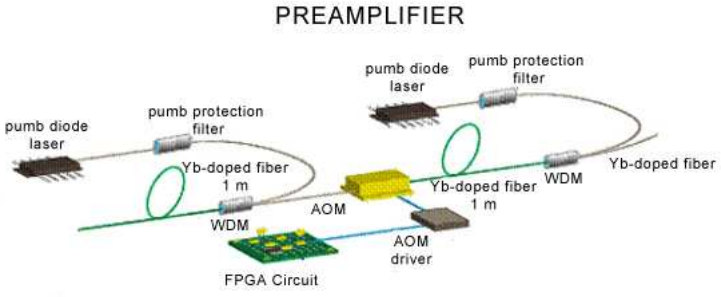

Figure 3.3. Schematic of the Pre-amplifier Setup.

The repetition frequency of the laser can be adjusted between 50 kHz and 3.1 MHz via the FPGA circuit. Figure 3.4 shows the schematics and logic of circuit.

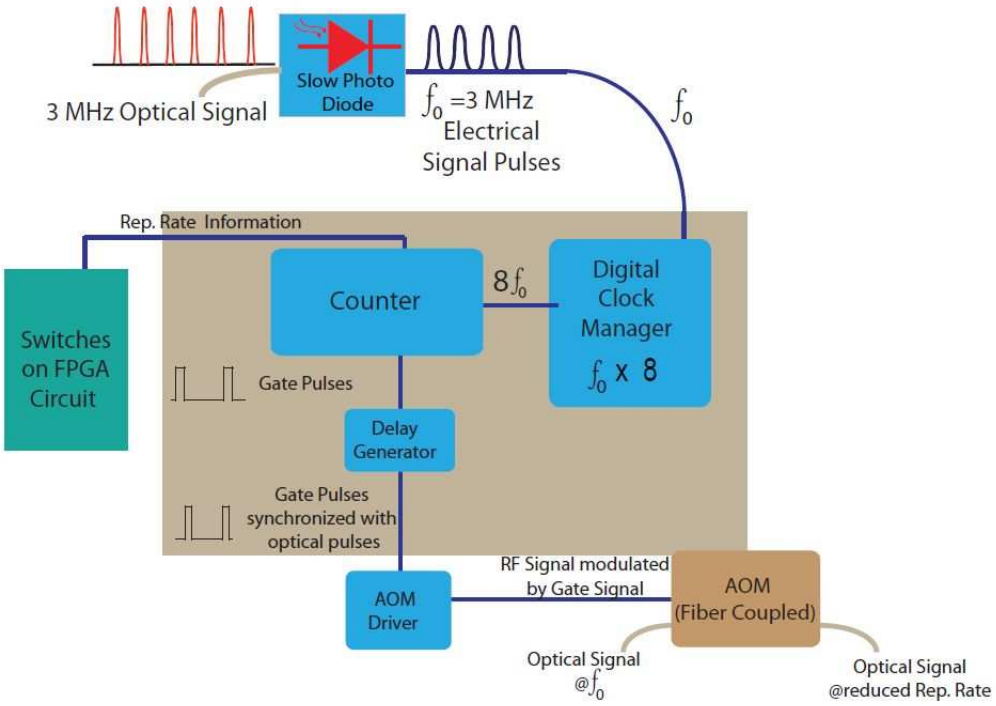

Figure 3.4. The Schematics of Field Programmable Gate Array (FPGA).

3.3.3. Final Amplifier

A 105 μm core multimode fiber coupled 976 nm diode laser of delivering a maximum power of 10 W is used as a pump source. The amplifier also includes 2 m long wide band double-clad Yb-doped fiber with 20 μm core diameter and numerical aperture of 0.07. The octagonal clayed fiber of the power amplifier has 125 μm core diameter and numerical aperture of 0.46. Figure 3.5 shows the schematics of the final amplifier.

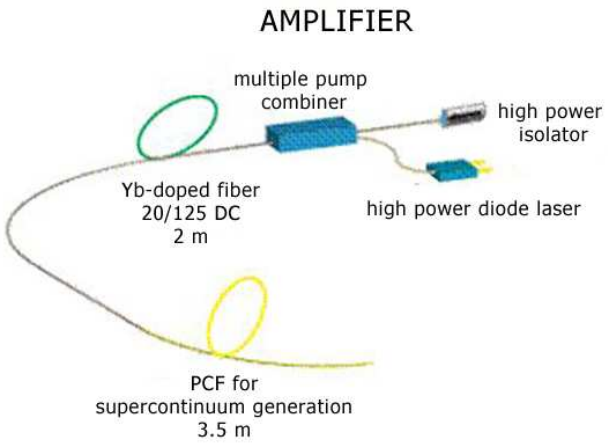

Figure 3.5. Schematics of Final Amplifier.

The optical power can be increased up to 1.8 W and the protection of the pre-amplifier is ensured by high-power isolator. Figure 3.6 shows the optical spectrum and the pulse duration of the laser before supercontinuum generation.

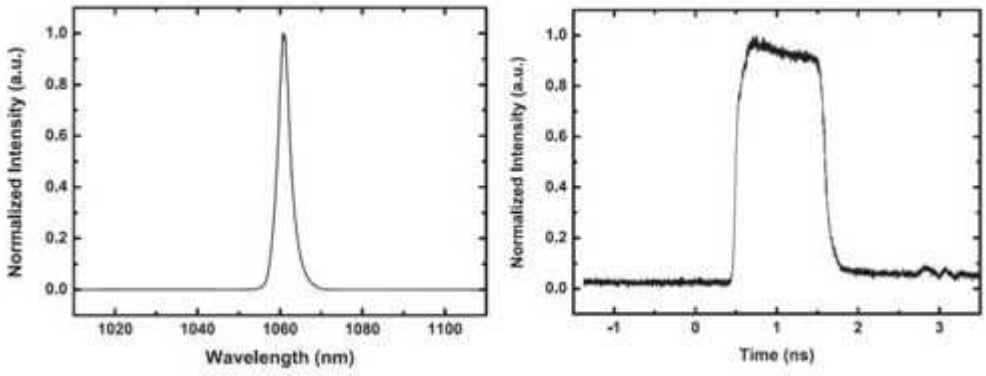

Figure 3.6. Schematics of Fiber Laser System.

3.3.3.1. Supercontinuum Generation. A 3.5 meter long photonic crystal fiber is spliced to double-clad Yb-doped fiber of the final amplifier for supercontinuum generation. The power delivery between wide band fiber to photonic cyristal fiber is around 35%; thus, the output power is 600 mW corresponding to 6 μJ pulse energy. "Nonlinear optical propagation is dramatically enhanced in a PCF due to its air silica honeycomb-like microstructure" [58]. The zero dispersion wavelength of the PCF is 1040 nm. As a result of non-linear effects, the spectrum broadens and supercontinuum between 600-1100 nm is generated. Figure 3.7 shows supercontinuum spectrum.

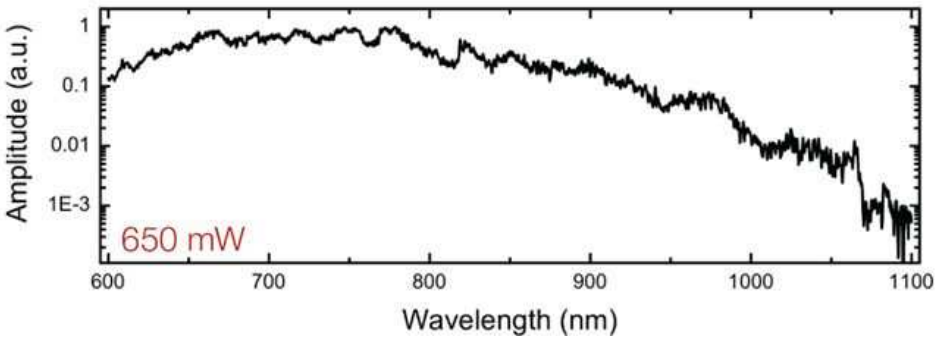

Figure 3.7. Supercontinuum Spectrum.

Figure 3.8 shows the light that seems yellow and dominantly red since the wavelengths in the supercontinuum correspond to that colors in the visible range of electromagnetic spectrum.

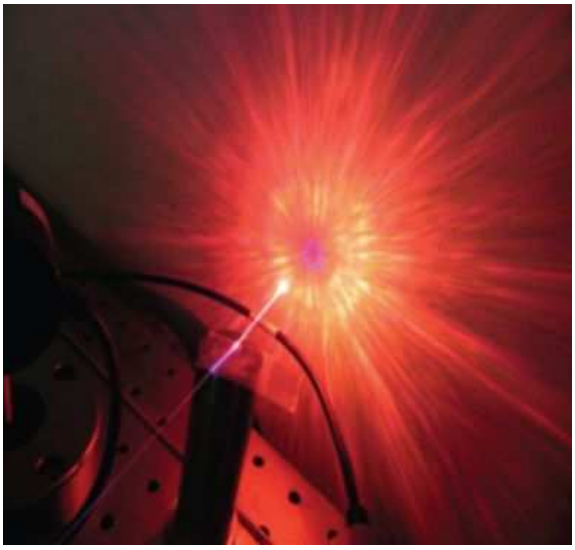

Figure 3.8. Generated Supercontinuum.

Figure 3.9 shows the laser system which is boxed in plexiglass for stability during experiments.

Figure 3.9. Picture of Fiber Laser System.

Filtering is required to excite different probes of interest such as hemoglobin, oxgenated hemoglobin, etc. Adjusting the central wavelength, acusto-optic modulator can be used as band filter for the purpose. Wavelength selection is also possible with optical filters of several wavelengths. By means of optical filters, probes can be exposed to multiple wavelengths. The image is formed by scanning sample with galvo-scanner at the end of acusto-optic modulator or the filters.

4. PHOTOACOUSTIC MICROSCOPY

4.1. Ultrasound System

In order to analyze ultrasound signal induced by laser, pulser/receiver (OLYMPUS 5073PR), pre-amplifier (OLYMPUS 5678) and data acquisition card (Gage, Express Compu Scope 1422) is used. Figure 4.1. shows pulse/echo signal received from data acquisition card.

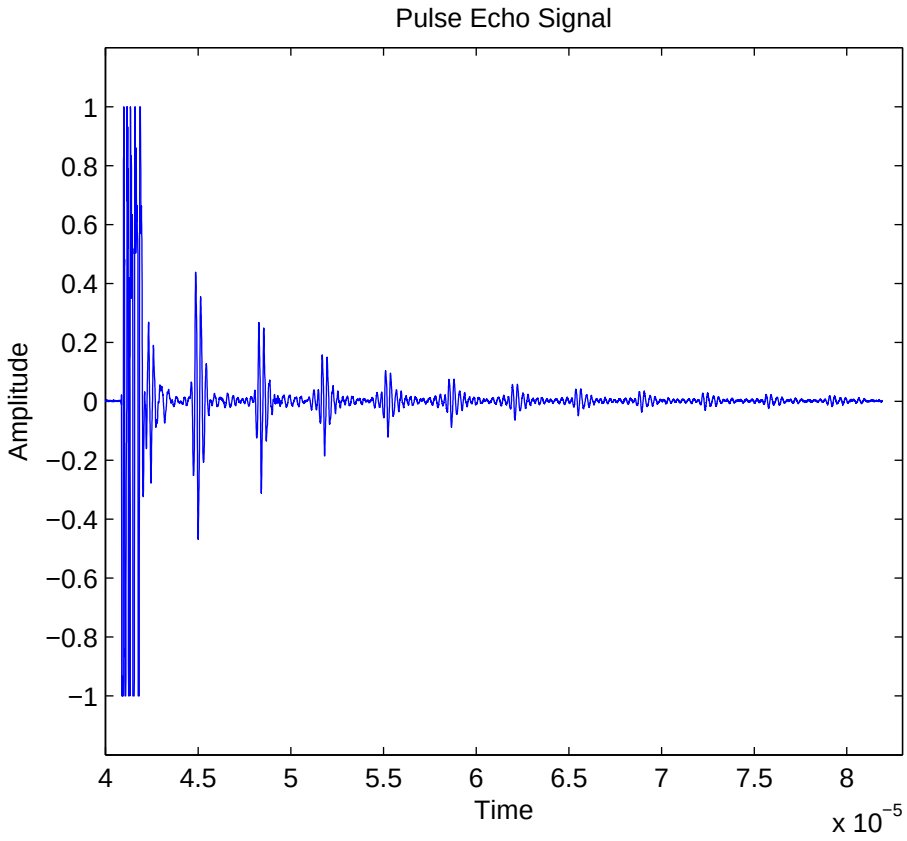

Figure 4.1. Pulse-Echo signal.

Figure 4.2 shows cable connections for Pulse-Echo operation of Pulser/Receiver with Oscilloscope.

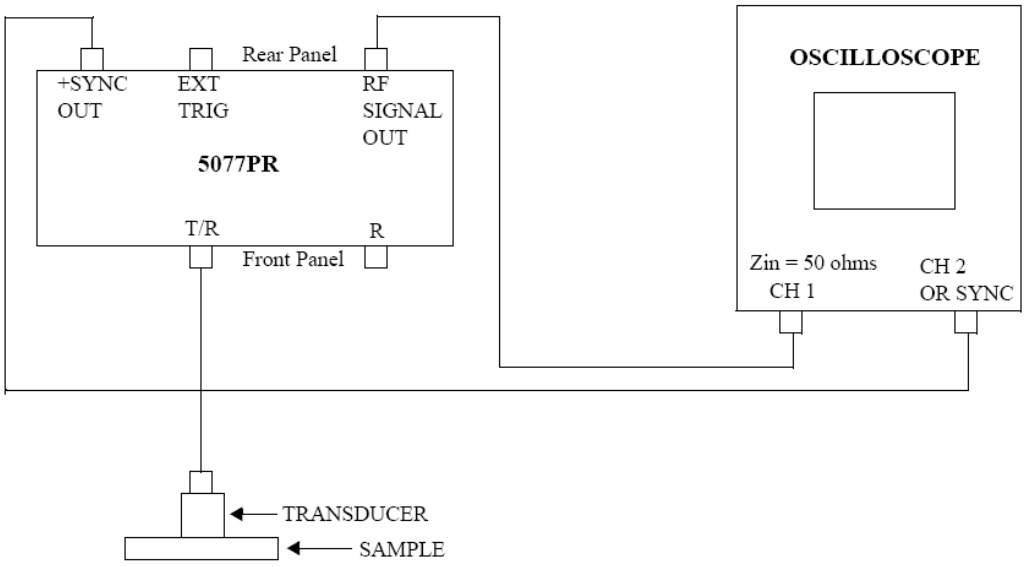

Figure 4.2. Cable connections for Pulse-Echo operation of Pulser/Receiver with Oscilloscope.

Figure 4.3 shows the pictures of pulser/receiver and pre-amplifier and Figure 4.4 shows initial oscilloscope and pulser/receiver settings.

Figure 4.3. Pulser/Receiver and Pre-Amplifier.

Oscilloscope	**Pulser/Receiver**
Vertical Sensitivity: 0.2V/Div	Mode: Position 1 (Pulse Echo)
Horizontal Sweep Rate: 1uS/Div	Rep Rate: 2K or 5K
Ext. Trig: Positive Slope	Pulser Voltage = 100V
	Transducer Frequency, according to chosen transducer
	Gain: -10dB
	HPF: OUT
	LPF: Full BW

Figure 4.4. Oscilloscope and Pulser/Receiver settings.

Figure 4.5 shows data acquisition card for very fast imaging.

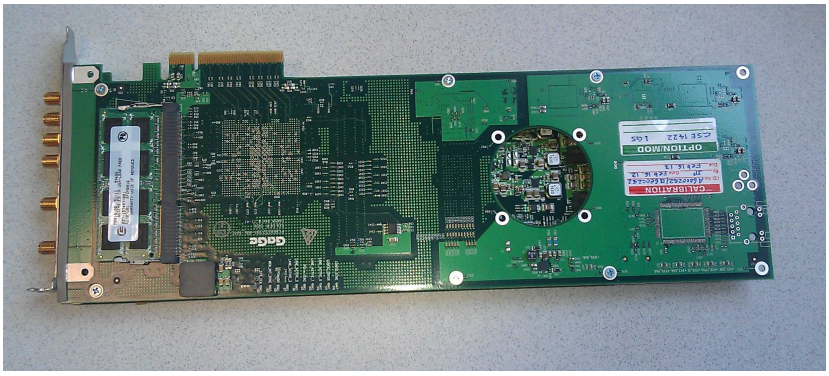

Figure 4.5. Data Acquisition Card.

4.2. System Design

Figure 4.6 shows the total laser system integrated with acusto-optic tunable filter and galvo scanner.

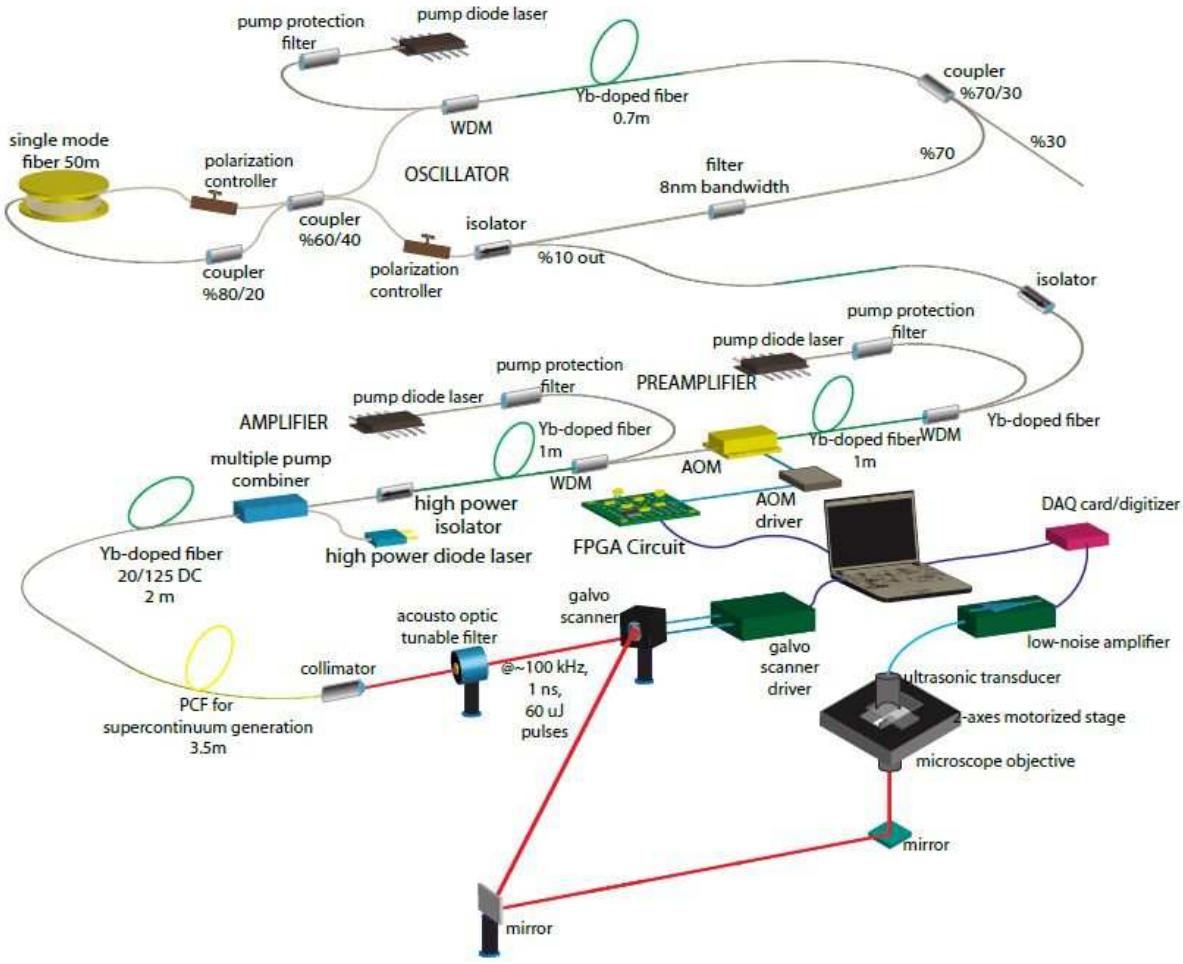

Figure 4.6. Schematics of PAM System.

5. CONCLUSION

The photoacoustic signal is a decreasing function of the pulse duration for constant pulse energy. For a particular wavelength, i.e., constant absorption coefficient, the amplitude of PA signal decreases with increased pulse duration provided that pulse energy is constant. In addition to this, when the pulse duration gets a larger value than the acoustic confinement time or the thermal confinement time, then the photoacoustic equation is no longer valid. The other way round, shorter pulse duration yields bigger photoacoustic wave amplitude. This condition holds as long as pulse duration allows light to be only linearly absorbed. For durations around picoseconds or femtoseconds, thermal and photoacoustic effects diminishes, intensity dependent non-linear laser tissue interactions occur. As a non-linear effect, two photon absorption cause tissue damage. Short pulse durations generates sound waves of higher frequency, so acoustic attenuation should be taken into consideration. Whensoever acoustic effects are also considered, the overall efficiency is still higher for shorter pulse durations.

As the ratio of radius of spherical object that is exposed to laser beam over beam width increases, the change of the normalized signal decreases slightly because the radial profile becomes very sharp and behaves like a Dirac delta function so that the laser parameters (pulse duration and beam width) begin to loose their effects on the signal.

When the average power of the laser is constant, decreasing pulse repetition frequency results in an increase in the energy so that the amplitude of the signal increases since the photoacoustic wave is proportional to the fluence and hence the energy of the laser. It should also be taken into consideration that the decrease in PRF results in slow data aquisition speed. On the other hand, high PRF can improve the contrast to-noise ratio (CNR) when weak contrast is imaged, since it allows extensive signal averaging.

PA signal amplitude is directly proportional to the local fluence and the absorption coefficient of the target. Therefore, taking measurements at multiple wavelengths allows for spectral separation of signals from different absorbers based on their characteristic absorption spectra and enables functional imaging.

Available lasers in the market have specific characteristics. Although, some have tunability over wavelength on the expense of energy, repetition frequency and pulse energy are usually constant. As a result of the constraints, lasers are chosen regarding the application. A laser suitable for melanoma cell detection with a wavelength of 1064 nm , e.g., is not appropriate for hemoglobin imaging since at the particular wavelength the absorption of hemoglobin is very low. Another laser with tunable wavelength may not be used for real time imaging because of having low PRF. Lasers having control over PRF, usually fiber lasers, have fixed wavelengths which is not suitable for spectroscopic measurements. Fixed energy obligates to perform microvasculature or celuluar imaging. In this thesis, the laser designed specifically for photoacoustics gives freedom to select wavelength between 600 nm and 1100 nm , energy between 2 nJ to 10 μJ, and repetition frequency between 50 kHz to 3 MHz; thus allows only one laser usage for many different applications.

REFERENCES

1. Dhawan, A. P., B. D'Alessandro, and X. Fu, "Optical Imaging Modalities for Biomedical Applications", *IEEE Reviews in Biomedical Engineering*, Vol. 3, pp. 69-92, 2010.

2. Acharya, R., R. Wasserman, J. Stevens, C. Hinojosa, "Biomedical Imaging Modalities: A Tutorial", *Computerized Medical Imaging and Graphics*, Vol. 19, pp. 3-25, 1995.

3. Boyd, N. F., G. A. Lockwood, J. Byng, D. L. Tritchler, and M. Yaffe, "Mammographic Densities and Breast Cancer Risk", *Cancer Epidemiology, Biomarkers and Prevention*, pp. 1133-1144, 1998.

4. Dhawan, A.P., *Medical Image Analysis*, IEEE Press, Wiley Interscience, New Jersey, NJ, USA, 2004.

5. Whaites, E., *Essentials of Dental Radiography and Radiology*, Churchill Livingstone, Edinburgh, 2002.

6. Kopans, D. B., *Breast Imaging*, Lippincott-Raven Publishers, Philadelphia, NY, 1998.

7. Brukilacchio, T. J., *A diffuse Optical Tomography Syste Combined with X-Ray Mammography for Improved Breast Cancer Detection*, Ph.D. Thesis, Harvard University, 2003.

8. Chacko, S., and M. Singh, "Three Dimensional Reconstruction of Transillumination Tomographic Images of Human Breast Phantoms by Red and Infrared Lasers", *IEEE Transactions on Biomedical Engineering*, pp. 131-135, 2000.

9. Cerussi, A. E., A. J. Berger, F. Bevilacqua, N. Shah, D. Jakubowski, J. Butler, R.

F. Holcombe, and B. J. Tromberg, "Sources of Absorption and Scattering Contrast for Near-Infrared Optical Mammography", *Academy of Radiology Research*, pp. 211-218, 2001.

10. Cooper, C. E., E. E. Elwell, J. H. Meek, S. J. Matcher, J. S. Wyatt, M. Cope, and D. T. Delpy, "The Noninvasive Measurement of Absolute Cerebral Deoxyhaemoglobin Concentration and Mean Optical Path Length in the Neonatal Brain by Second Derivative Near Infrared Spectroscopy", *Pediatric Research*, pp. 32-38, 1996.

11. Conway, J. M., K. H. Norris, and C. E. Bodwell, "A New Approach for the Estimation of Body Composition: Infrared Interactance", *The American Journal of Clinical Nutrition*, pp. 1123-1130, 1984.

12. Roggan, A., M. Friebel, K. Dörschel, A. Hahn, and G. Müller, "Optical Properties of Circulating Human Blood in the Wavelength Range 400-2500 nm", *Journal of Biomedical Optics*, pp. 36-46, 1999.

13. Wang, L. V., "Ultrasound-Mediated Biophotonic Imaging: A review of Acoustooptical Tomography and Photoacoustic Tomography", *Disease Markers*, pp. 123- 138, 2004.

14. Kim, C., T. Erpelding, L. Jankovic, M. Pashley, and L. Wang, "Deeply Penetrating in Vivo Photoacoustic Imaging Using a Clinical Ultrasound Array System", *Biomedical Optics Express*, pp. 278-284, 2010.

15. Zhao Q., L. Ji, and T. Jiang, "Improving Depth Resolution of Diffuse Optical Tomography with a Layer-Based Sigmoid Adjustment Method", *Optics Express*, Vol. 15, pp. 4018-4029, 2007.

16. Enfield, L. C., A. P. Gibson, J. C. Hebden, and M. Douek, "Optical Tomography of Breast Cancer Monitoring Responseto Primary Medical Therapy", *Target Oncology*, pp. 219-33, 2009.

17. Pogue, B. W., S. C. Davis , X. Song , B. A. Brooksby, H. Dehghani ,K. D. Paulsen, "Image Analysis Methods for Diffuse Optical Tomography", *Journal of Biomedical Optics*, Vol. 11, p. 033001, 2006.

18. Franceschini, M. A., K. T. Moesta , S. Fantini, G. Gaida, E. Gratton , J. H. Helge, W. W. Mantulin, M. Seeber, P. M. Schlag, M. Kaschke, "Frequency-Domain Techniques Enhance Optical Mammography: Initial Clinical Results", *Proceedings of the National Academy of Sciences*, pp. 6468-6473, 1997.

19. Kießling, F., and B.J. Pichler, *Small Animal Imaging: Basics and Practical Guide*, Springer, New York, NY, USA, 2011.

20. Wang, L. V., "Tutorial on Photoacoustic Microscopy and Computed Tomography", *IEEE Journal of Selected Topics on Quantum Electronics*, pp. 171-179, 2008.

21. Zhang, Y., H. Hong, W. Cai, "Photoacoustic Imaging", *Cold Spring Harb Protocols*, 2011.

22. Beckmann, N., "In Vivo Magnetic Resonance Techniques and Drug Discovery", *Brazilian Jounal of Physics*, , Vol. 36, pp. 16-22, 2006.

23. Jiechen, Y., "Photoacoustic tomography in Cancer Detection", 2012, http://bme240.eng.uci.edu/students/08s/jiecheny/index.htm, accessed at August 2012.

24. Lüscher, E. , *Photoacoustic Effect: Principles and Applications*, Braunschweig: Friedr. Vieweg and Sohn, Germany, 1984.

25. Tam, A. C., "Applications of Photoacoustic Sensing Techniques", *Revievs of Modern Physics*, pp. 381-431, 1986.

26. Allen, T. J., B. T. Cox, P. C. Beard, "Generating Photoacoustic Signals Using High-Peak Power Pulsed Laser Diodes", *Proceedings of the International Society for Optics and Photonics*, pp. 233-242, 2005.

27. Salehin, S. M. A., and T. D. Abhayapala, "Signal Processing and Communication Systems", *International Conference on Signal Processing and Communication Systems*, 2010.

28. Gusev, V. E., and A. A. Karabutov, *Laser Optoacoustics*, NewYork, NY, USA, 1992.

29. Wang, L. V., and H.I. Wu, *Biomedical Optics*, Wiley, New Jersey, NJ, USA, 2007.

30. Frenz, M., G. Paltauf and H. Schmidt-Kloiber, "Laser-Generated Cavitation in Absorbing Liquid Induced by Acoustic Diffraction", *Physical Reviev Letters*, Vol.76, pp. 3546-3549, 1996.

31. Wang, L. V., "Prospects of Photoacoustic Tomography", *Medical Physics*, Vol. 35, pp. 5758-5767 , 2008.

32. Krumholz, A., S. J. VanVickle-Chavez, J. Yao, T. P. Fleming, W. E. Gillanders and L. V. Wang, "Photoacoustic Microscopy of Tyrosinase Reporter Gene in Vivo", *Journal of Biomedical Optics*, Vol. 16, 2011.

33. Beard, P., "Biomedical Photoacoustic Imaging", *Interface Focus*, Vol. 1, No. 4, pp. 602-631, 2011.

34. Hu, S., K. Maslov, and L. V. Wang, "In Vivo Functional Chronic Imaging of a Small Animal Model Using Optical-Resolution Photoacoustic Microscopy", *Medical Physics*, Vol. 36, No. 6, pp. 2320-2323, 2009.

35. Zhang, H. F., K. Maslow, G. Stocia, and L. V. Wang, "Functional Photoacoustic Microscopy for High Resolution and Noninvasive in Vivo Imaging", *Nature Biotechnology*, Vol. 24, No. 7, pp. 848-851, 2006.

36. Yao, J., K. Maslow, Y. Zhang, and L. V. Wang, "Label-Free Oxygen Metabolic Photoacoustic Microscopy in Vivo" , *Journal of Biomedical Optics*, Vol. 16, No. 7, 2011.

37. Krumholz, A., L. V. Wang, J. Yao, and L.V. Wang, "Functional Photoacoustic Microscopy of Diabetic Vasculature", *Journal of Biomedical Optics*, Vol. 17, 2012.

38. Yvonne-Tee, G. B., A. H. Rasool, A. S. Halim, and A. R. Rahman, "Noninvasive Assessment of Cutaneous Vascular Function in Vivo Using Capillaroscopy, Plethysmography and Laser-Doppler Instruments: Its Strengths and Weaknesses", *Clinical Hemorheology and Microcirculation*, Vol. 34, No. 4, pp. 457- 473, 2006.

39. Favazza, C. P., L. A. Cornelius, and L. V. Wang, "In Vivo Functional Photoacoustic Microscopy of Cutaneous Microvasculature in Human Skin", *Journal of Biomedical Optics*, Vol. 16, No. 2, 2011.

40. Addor, G., A. Delachaux, B. Dischi, D. Hayoz, L. Liaudet, B. Waeber, and F. Feihl, "A Comparative Study of Reactive Hyperemia in Human Forearm Skin and Muscle", *Physiological Research*, Vol. 57, No. 5, pp. 685-692, 2008.

41. De Mul, F. F., F. Morales, A. J. Smit, and R. Graaff, "A model for Postocclusive Reactive Hyperemia as Measured with Laser-Doppler Perfusion Monitoring," *IEEE Transactions on Biomedical Engineering*, Vol. 52, No. 2, pp. 184-190, 2005.

42. Cheatle, T. R., L. A. Potter, M. Cope, D. T. Delpy, P. D. Coleridge Smith, and J. H. Scurr, "Near-Infrared Spectroscopy in Peripheral Vascular Disease", *British Journal and Surgery*, Vol. 78, No. 4, pp. 405-408, 1991.

43. Andreassen, A. K., K. Kvernebo, B. Jorgensen, S. Simonsen, J. Kjekshus, and L. Gullestad, "Exercise Capacity in Heart Transplant Recipients: Relation to Impaired Endothelium-Dependent Vasodilation of the Peripheral Microcirculation", *American Heart Journal*, Vol. 136, No. 2, pp. 320-328, 1998.

44. Stein, E. W., K. Maslov, and L. V. Wang, "Noninvasive, in Vivo Imaging of The Mouse Brain Using Photoacoustic Microscopy", *Journal of Applied Physics* , Vol. 105, No. 10, 2009.

45. Hunt, T. K., B. Zederfeldt, T. K. Goldstick, "Oxygen and healing", *American Heart Journal*, Vol. 118, pp. 521-525, 1969.

46. Hu, S., K. Maslov, and L. V. Wang, "In Vivo Functional Chronic Imaging of a Small Animal Model Using Optical-Resolution Photoacoustic Microscopy", *Medical Physics*, Vol. 36, No. 6, pp. 2320-2323, 2009.

47. Christensen, D.A., *Ultrasonic Bioinstrumentation*, Wiley, New York, NY, USA, 1988.

48. Wells, P. N. T., "Ultrasonic Imaging of The Human Body", *Reports on Progress in Physics*, Vol. 62, pp. 671-722, 1999.

49. Anthony, R. M., M. J. Fitzpatrick, D. E. Neal,J. R. N. George, *The Scientific Basis of Urology*, Taylor and Francis, London, England, 2004.

50. Morse, P. M. and H. Feshbach, *Methods of Theoretical Physics, Part I*, McGraw-Hill, 1953.

51. Li, C and Wang L. V., "Photoacoustic Tomography and Sensing In Biomedicine", *Physics in Medicine and Biology*, Vol. 54, No. 19, 2009.

52. Zhang, C., Y. Cheng, J. Chen , S. Wickline and Wang L.V., "Label-Free Photoacoustic Microscopy of Myocardial Sheet Architecture", *Journal of Biomedical Optics*, Vol. 17, No. 6, 2012.

53. Yeh, C., S. Hu , K. Maslov, and L. V. Wang, "Photoacoustic Microscopy of Blood Pulse Wave", *Journal of Biomedical Optics* , Vol. 17, 2012.

54. Saka, M., J. Berwick, M. Jones, "Linear Superposition of Sensory-Evoked and Ongoing Cortical Hemodynamics", *Frontiers in Neuroenergetics*, pp. 1662-6427, 2010.

55. Favazza, C. P., L. A. Cornelius, and L. V. Wang, "In Vivo Functional Photoacoustic

Microscopy of Cutaneous Microvasculature in Human Skin", *Journal of Biomedical Optics*, Vol. 16, No. 2, 2011.

56. Yao, J., K. I. Maslov, Y. Zhang, Y. Xia, L. V. Wang, "Label-free Oxygen-metabolic Photoacoustic Microscopy in Vivo", *Journal of Biomedical Optics*, Vol. 16, No. 7, p. 076003, 2011.

57. Jo, J. and Yang, X., "Functional Photoacoustic Imaging to Observe Regional Brain Activation Induced by Cocaine Hydrochloride", Journal of Biomedical Optics, Vol. 16, 090505 (2011).

58. Liu, M. and T. Buma, "Wavelength Agile Photoacoustic Microscopy with a Pulsed Supercontinuum Source", IEEE, 2010.

59. Liao, L. D., M. L. Li , H. Y. Lai , Y. Y. Shih, Y. C. Lo , S. Tsang, C. P. Chao, C. Y. Lin, F. S. Jaw, Y. Y. Chen, "Imaging Brain Hemodynamic Changes During Rat Forepaw Electrical Stimulation Using Functional Photoacoustic Microscopy", *Neuroimage*, Vol. 52, No. 2, pp. 562-70, 2010.

60. Yang, S., F. Ye, D. Xing, "Intracellular Label-Free Gold Nanorods Imaging with Photoacoustic Microscopy", *Optics Express*, Vol. 20, pp. 10370-10375, 2012.

61. Staley, J., P. Grogan , A. K. Samadi , H. Cui, M. S. Cohen, X. Yang, "Growth of Melanoma Brain Tumors Monitored by Photoacoustic Microscopy", *Journal of Biomedical Optics*, Vol. 15, No. 4, 2010.

62. Wang, Y., K. Maslov, Y. Zhang, S. Hu, L. Yang, Y. Xia, J. Liu, and L. V. Wang, "Fiber Laser Based Photoacoustic Microscopy and Melanoma Cell Detection", *Journal of Biomedical Optics* , Vol. 16, 2011.

63. Shi, W., P. Hajireza, P.Shao, A. Forbrich, and R. J. Zemp, "In vivo Near-Realtime Volumetric Optical-resolution Photoacoustic Microscopy Using a High-repetition-rate Nanosecond Fiber-laser", *Optics Express*, Vol. 19, pp. 17143-17150, 2011.

64. Shao, P., W. Shi, R. K. Chee, and R. J. Zemp, "Mosaic Acquisition and Processing for Optical-Resolution Photoacoustic Microscopy", *Journal of Biomedical Optics*, Vol. 17, p. 080503, 2012.

65. Zeng, L., G. Liu, D. Yang, X. Ji, "3D-visual Laser Diode Based Photoacoustic Imaging", *Optics Express*, Vol. 20, No. 2, p. 1237, 2012.

66. Özgören, K., B. Öktem, S. Yılmaz, F. Ö. İlday, K. Eken, "83 W, 3.1 MHz, Square-Shaped, 1 ns Pulsed All Fiber Integrated Laser for Micromachining," *Optics Express 19*, pp. 17647-17652, 2011.

67. Pachotta, R., "Encyclopedia of Laser Physics and Technology", 2011, http://www.rp-photonics.com/acousto-optic-modulators.html, accessed at May 2012.